Journal: Molecular Psychiatry

Revised: Dec. 14th, 2023

EF1α-associated Protein Complexes Affect Dendritic Spine Plasticity by Regulating Microglial Phagocytosis in *Fmr1* Knock-out Mice

Running Title**:** TRIM3-EF1α-Mdm2 complex in fragile X syndrome

[1]Ping Su, [1]Shuxin Yan, [2]Kai Chen, [3]Lianyan Huang, [4]Le Wang, [1]Frankie Hang Fung Lee, [2]Hang Zhou, [1,5]Terence Kai Ying Lai, [1]Anlong Jiang, [1]James Samsom, [1,6.7,8]Albert H.C. Wong, [2]Guang Yang and [1, 4, 5,6,8,9] Fang Liu

[1]Campbell Family Mental Health Research Institute,
Centre for Addiction and Mental Health,
[2]Department of Anesthesiology, Columbia University Medical Center,
New York, NY10032, USA
[3]Department of Anesthesiology, New York University School of Medicine,
New York, NY10016, USA.
[4]Institute of Mental Health and Drug Discovery, Oujiang Laboratory
(Zhejiang Lab for Regenerative Medicine, Vision and Brain Health), School of Mental Health,
Wenzhou Medical University, Wenzhou, Zhejiang, 325000, China
[5]Department of Physiology, [6]Psychiatry, [7]Pharmacology and Toxicology and [8]Institutes of Medical Science, University of Toronto,
Toronto, Ontario, M5T 1R8 Canada

[9]**ADDRESS FOR CORRESPONDENCE:**
Fang Liu, M.D., Ph.D.
Campbell Family Mental Health Research Institute
Centre for Addiction and Mental Health
250 College Street
Toronto, Ontario M5T 1R8
Tel. (416) 979-4659
Fax (416) 979-4663
E-mail: fang.liu@camh.ca

Abstract

Fragile X syndrome (FXS) is the most common inherited cause of intellectual disability. There is no specific treatment for FXS due to the lack of therapeutic targets. We report here that Elongation Factor 1α (EF1α) forms a complex with two other proteins: Tripartite motif-containing protein 3 (TRIM3) and Murine double minute (Mdm2). Both EF1α-Mdm2 and EF1α-TRIM3 protein complexes are increased in the brain of *Fmr1* knockout mice as a result of FMRP deficiency, which releases the normal translational suppression of EF1α mRNA and increases EF1α protein levels. Increased EF1α-Mdm2 complex decreases PSD-95 ubiquitination (Ub-PSD-95) and Ub-PSD-95-C1q interaction. The elevated level of TRIM3-EF1α complex is associated with decreased TRIM3-Complement Component 3 (C3) complex that inhibits the activation of C3. Both protein complexes thereby contribute to a reduction in microglia-mediated phagocytosis and dendritic spine pruning. Finally, we created a peptide that disrupts both protein complexes and restores dendritic spine plasticity and behavioural deficits in *Fmr1* knockout mice. The EF1α-Mdm2 and EF1α-TRIM3 complexes could thus be new therapeutic targets for FXS.

Introduction

FXS results from a mutation in the fragile x mental retardation (*FMR1*) gene, leading to insufficiency of the fragile x mental retardation protein (FMRP) [1, 2]. FXS includes a spectrum of clinical manifestations, from learning disabilities to severe intellectual disability. Current treatment for FXS consists of special education programs and therapy for speech, physical, or behavioural problems [3]. Medications are used to treat FXS-associated conditions such as seizures, mood dysregulation, hyperactivity, and attention deficits, but there is currently no specific molecular target for pharmacological treatment of FXS [4, 5].

Neuron dendritic spine density is increased in both patients with FXS and *Fmr1* knock-out (KO) mice [6-8] as well as some types of Autistic Spectrum Disorder (ASD) [9]. Most spines have an elongated immature morphology, suggesting a deficit in excitatory synapse elimination [10]. FMRP has a central role in synapse structure and function, interacting with almost one third of synaptic mRNAs [11]. In this paper, we investigate protein-protein interactions with FMRP that regulate dendritic spine density and affect behaviours relevant to the clinical manifestations of FXS in humans.

FMRP is an RNA-binding protein that regulates the translation of target mRNAs [11, 12]. FMRP binds to eukaryotic translation elongation factor 1-α (EF1α) mRNA and suppresses its translation [13]. In *Fmr1* KO mice, loss of FMRP releases the normal translational suppression of EF1α mRNA, thereby increasing EF1α protein levels [11, 13]. EF1α channels aminoacyl tRNAs to the ribosome for peptide chain elongation [14, 15]. EF1α mRNA is localized in dendrites and translated in conjunction with long-term depression [16]. EF1α is expressed in many tissues outside of the brain, functioning as a transcription elongation factor, a GTPase, and an actin bundling protein that is involved in cancer, muscle disorders, cardiovascular disease and development [17-20].

Excess EF1α binds to and sequesters murine double minute2 (Mdm2), a ubiquitin E3 ligase [21]. This sequestration of Mdm2 plays a role in MEF2 (myocyte enhancer factor 2)-induced functional synapse elimination through inhibiting PSD95 ubiquitination and dephosphorylation of Mdm2, both of which contribute to aberrant synapse density [22, 23].

TRIM3 (Tripartite motif-containing protein 3) is a predominantly neural member of the TRIM-NHL family of proteins that regulates aspects of development including cell growth, proliferation and differentiation [24]. As the name implies, TRIM3 contains three interacting domains that form the basis of its function: Really Interesting New Gene (RING) finger, B-Box-type zinc fingers (BB1 and BB2) and a Coiled-Coil (CC) region. The RING domain can act as an ubiquitin E3 ligase, and there are also similarities between the BB domains and the structure of ubiquitin E3 ligases [25]. TRIM3 interacts with neuronal myosin V as part of the CART (Cytoskeleton-Associated Recycling or Transport) complex involved in membrane receptor recycling, specifically the $GABA_A$ receptor [26]. TRIM3 is also a tumor suppressor [27], including for gliomas [28], and has previously been implicated in modulating dendritic spine morphology [29]. Increased TRIM3 protein levels have been observed in post-mortem brain tissue from patients with schizophrenia [30].

The C3 protein is a core component of the complement cascade, a molecular effector of the immune system for inflammation and cellular destruction. C3 is cleaved by C3-convertase into C3a and C3b, then C3b binds to pathogens marking them for phagocytosis [31]. In addition to this classical function in combating infection, the complement cascade and microglia also perform analogous functions in normal development, consuming and removing unwanted dendritic spines [32, 33]. Another key player in synaptic spine elimination is Protocadherin-10 (Pcdh10), a member of the cadherin superfamily of calcium-dependent cell adhesion molecules. Ub-PSD-95 is

delivered by Pdch10 to the proteasome, which then acts to degrade PSD-95 [22, 23]. MEF2 activation promotes the association of Pcdh10 with PSD-95, which is deficient in cultured neurons derived from *Fmr1* KO mice [22, 34]. Thus, we predict that Ub-PSD-95 binding with Pcdh10 will be lower in *Fmr1* KO mice compared to wild-type (WT) mice.

In this paper, we sought to investigate protein-protein interactions between TRIM3, EF1α and Mdm2, and their impact on dendritic spine dynamics and behaviour in the *Fmr1* KO mouse. The literature reviewed above suggests potential functional links between these proteins that could be exploited to develop new drugs that target the underlying molecular pathophysiology of FXS. In the sections that follow, we present evidence for the existence of a three-way TRIM3-EF1α-Mdm2 protein interaction. We have identified the binding regions for these interactions and developed a small peptide that can block these interactions and rescue molecular, cellular and behavioural abnormalities in *Fmr1* KO mice.

Materials and Methods

Study design

The aim of this project was to investigate the mechanisms that the identified EF1α-associated protein complex affects dendritic spine plasticity in *Fmr1* knock-out mice. Biological triplicates or quadruplicates were used for *in vitro* experiments, co-immunoprecipitation, GST pull-down, western blot, Glogi-Cox staining, immunohistochemistry (n =3-4 mice per group). *In vivo* dendritic spine imaging was performed using a two-photon microscope (n=5-6 mice per group) (detailed methods below). Animals were treated from P14 to P20 via intraperitoneal (*i.p.)* injections, and behaviors were tested at 8 weeks-of-age (please find detailed timeline in supplementary information). Mice of both sexes were randomized to each group before injection

(n = 8 mice per group). Sample sizes (both *in vitro* and *in vivo*) were chosen according to similar tests in our previous publications. No data were excluded in all experiments. Treatment groups were blinded for Golgi-Cox staining and animal behavioural analyses. All animal procedures were performed with approval from Animal Care Committee at the Centre for Addiction and Mental Health or Columbia University.

Peptides and drugs

TAT-EF1α or TAT peptide was dissolved in ddH_2O to a stock solution of 10 mM. Mice were injected with 3 nmol/g of TAT-EF1α or TAT peptide diluted in 0.9% saline to make a final injection volume of 50 μl per mouse. Nutlin-3 (Selleck Chemicals, Houston, TX, Cat# S1061) was dissolved in ethanol to a stock solution of 5 mM.

GST fusion protein constructs

GST-fusion proteins encoding truncated EF1α fragments were amplified by PCR from full-length human cDNA clones (Origene Technologies). All constructs were sequenced to screen for PCR-generated nucleotide errors. GST-fusion proteins were prepared from bacterial lysates with Glutathione Sepharose 4B beads following manufacturer instructions (Amersham). To construct GST-fusion proteins encoding truncated EF1α, cDNA fragments were amplified by PCR with specific primers. Except where specified, all 5' and 3' oligonucleotides incorporated BamHI sites (GGATCC) and XhoI sites (CTCGAG) (New England Biolabs), respectively, to facilitate sub-cloning into the pGEX-4T3 vector. All constructs were re-sequenced to confirm appropriate splice fusion and the absence of spurious PCR generated nucleotide errors.

Co-immunoprecipitation, protein affinity purification and Western Blot

Co-immunoprecipitation, protein affinity purification, and Western Blot analyses were performed as previously described [35-37]. For co-immunoprecipitation experiments, 500~700 μg of

solubilized protein extracted from mouse brain tissue was incubated in the presence of protein A/G plus agarose (Santa Cruz Biotechnology) for 12 hrs. Pellets were washed, boiled for 5 min in SDS sample buffer (Bio-Rad) and subjected to SDS-PAGE. 10~50 μg of protein extracted from tissue was used as a control in each experiment. For protein affinity purification experiments, 500~700 μg of protein was incubated with glutathione-sepharose beads (Amersham) bound to the indicated GST-fusion proteins (50~100 μg) at 4°C overnight. Beads were washed, boiled for 5 min in SDS sample buffer, and subjected to SDS-PAGE. After transfer of proteins onto nitrocellulose, membranes were Western blotted with the primary antibodies specified below. The intensity of protein level was quantified by densitometry (software: Image J, NIH).

The antibodies used were anti-EF1α (Abcam, rabbit, catalog #ab157455), anti-Mdm2 (Novus Biologicals, rabbit, catalog #NBP2-17247), anti-PSD95 (Abcam, rabbit, catalog #ab238135), anti-TRIM3 (Santa Cruz Biotechnology, mouse, catalog #sc-136363), normal rabbit IgG (Millipore, rabbit, catalog #12-370), and normal mouse IgG (Santa Cruz Biotechnology, mouse, catalog #sc-2025) for immunoprecipitation; anti-EF1α (Millipore, mouse, catalog #05-235), anti-Mdm2 (Santa Cruz Biotechnology, mouse, catalog #sc-965), anti-TRIM3 (Santa Cruz Biotechnology, mouse, catalog #sc-136363), anti-PSD95 (Abcam, rabbit, catalog #ab238135), anti-Ub (Millipore, rabbit, catalog #07-2130), anti-C1q (Abcam, rabbit, catalog #ab155052), anti-C3 (Abcam, rabbit, catalog #200999), anti-α-Tubulin (Sigma-Aldrich, mouse, catalog #T8203) for Western blot.

Cortical neuron primary cultures

Primary cultures of cortical neurons were generated as previously described [38]. Briefly, P0 C57BL/6 mice (both male and female mice) were anaesthetized by being placed on ice. After disinfection with 75% alcohol, mice were sacrificed by decapitation. The cerebral hemispheres were isolated and transferred to ice-cold Hank's buffer. The meninges and blood vessels were

removed and the cortex was dissected out. The cortex was then minced into approximately 1-mm pieces with curved scissors. The cortical tissues were digested in 2-3 ml 0.125% trypsin for 5 min, and then the trypsin was inactivated by adding cell culture medium (twice the volume of trypsin). Cells were dispersed by serial pipetting, then counted and seeded onto culture plates. Half the volume of the cell culture medium was replaced with new media every 3 days.

Trim3 siRNA treatment

Mouse Trim3 siRNA including a mixture of 4 siRNA (Accell mouse Trim3 siRNA SMARTpool, Dharmacon, catalog E-046341-00-005) and control siRNA (catalog D-001950-01) were purchased from Horizon Discovery (Lafayette, CO, USA). The 4 siRNA in the Accell mouse Trim3 siRNA are: Accell SMARTpool siRNA A-046341-13, Target sequence: GGUUGCACUUUAUUUAUUC; Accell SMARTpool siRNA A-046341-14, Target sequence: GUAUCAGCAACAAGUAGUG; Accell SMARTpool siRNA A-046341-15, Target sequence: CCAAUGUAUUCAGGUUUUC; Accell SMARTpool siRNA A-046341-16, Target sequence: GCUUUAAGGCCUAUCGAUA. Briefly, siRNA stock solution was diluted with Accell siRNA delivery media and added directly to primary cortical neuron cultures (1 nmol stock into 20 µl media for one well in a 12-well plate), and incubated for 72 hours.

Golgi-Cox staining

Golgi-Cox staining was performed as previously described [39]. Briefly, P21 mice were anesthetized with isoflurane and intracardially perfused with 0.9% saline. Brains were dissected and immersed in Golgi-Cox solution in the dark for 14 d before transfer to 30% sucrose solution for 5 d. Sections of 200 µm thick were sliced using a microtome (Leica VT1000S) and placed on 2% gelatinized microscope slides. The slides were stored in a humidified chamber before further staining and fixation.

Analysis of dendritic spine density in Golgi-Cox staining

Spine density was calculated from Golgi-Cox stained images captured at 100 × magnification (Nikon Eclipse E600). Only spines on the apical dendrites of pyramidal neurons in layers III and V of frontal cortex were counted. Spine density was defined as the number of spines per 10 μm of dendritic length. All image analysis was conducted blind to the treatment groups.

***In vivo* transcranial two-photon imaging of dendritic spines**

Mice

Thy1-YFP-H mice (stock 003782) and *Fmr1* KO mice were purchased from the Jackson Laboratory (Bar Harbor, ME, USA). To facilitate imaging of dendritic spine plasticity in *Fmr1* KO mice, these mice were crossed with *Thy1*-YFP-H mice. Both male and female mice were used, and were injected from P14 to P20. All mice were maintained at the Columbia University animal facility and handled in accordance with the institutional guidelines for animal care and use (In vivo studies of neural plasticity AC-AABN7553).

In vivo transcranial two-photon imaging

Dendritic spines in the frontal cortex were imaged through a thinned-skull window using a two-photon microscope. Briefly, surgical anesthesia was achieved using an intraperitoneal injection of 100 mg/kg ketamine and 15 mg/kg xylazine. A midline scalp incision exposed the skull. The area to be imaged was identified based on stereotaxic coordinates for the frontal association cortex (1.1 mm lateral from midline, 2.8 mm anterior from bregma). The head was immobilized, and a cranial window was created by thinning a circular area (~200 μm in diameter) of the skull to ~20 μm in thickness by using a high-speed drill and/or a microsurgical blade. After completion of the skull thinning, the animal was placed under a two-photon microscope while still

under anesthesia. The two-photon laser was tuned to 920 nm. All experiments were performed using a 1.1–numerical aperture (NA) 60× objective lens immersed in artificial cerebrospinal fluid to obtain high-magnification (66.7 μm × 66.7 μm; 512 × 512 pixels; 0.75-μm step) images for dendritic spine analysis. After imaging, the scalp was sutured with 6-0 silk, and the animal was returned to the home cage until the next viewing.

Imaging data analysis.

Analysis of dendritic spine plasticity was performed using the NIH ImageJ software, as described previously [40, 41]. Briefly, for each dendritic segment, filopodia were identified as long, thin protrusions without bulbous heads, and the remaining protrusions were classified as spines. Images of the same dendritic segments identified from two views were compared. Spines were considered stable if they were present in both views, eliminated if they were present in the first view but not in the second view, or were considered to be newly formed if they were present in the second view but not in the first view. The elimination and formation rates were measured as the number of spines eliminated or formed in the second view divided by the number of spines existing in the first view.

In vivo spine statistical analysis

Prism software (GraphPad 7.05, La Jolla, CA) was used to conduct the statistical analysis. Summary data are presented as mean ± s.e.m. Tests for differences among multiple groups were performed with one-way ANOVA followed by a Bonferroni's *post hoc* test as specified in the figure legends. No data points were excluded from the statistical analysis, and variance was similar between the groups being statistically compared. Significance was set at $P < 0.05$.

Animal behaviour test

Animals

Except mice used for *in vivo* dendritic spines imaging, both male and female adult wild-type mice were obtained from Charles River Farms (St. Constant, QC, Canada), and *Fmr1* KO mice were purchased from the Jackson Laboratory (stock number 003025) with each experiment performed on separate groups. Both male and female mice were used for injection from P14-P20, and littermates of the same sex were randomly assigned to experimental groups. A 12:12 h light–dark cycle was maintained with artificial light. All procedures were approved by the Centre for Addiction and Mental Health Animal Care Committee (protocol #705, #778, and #813).

Elevated Plus-Maze test

The elevated plus-maze consists of two open arms and two closed arms situated opposite each other, separated by a central platform. Animals were individually placed in the center square and allowed to move freely for 5 minutes. Arm entries were be defined as the mouse having all four paws within an arm. A digital video camera was used to record the movement of the animals in the maze. The number of entries and time spent in each arm were analyzed using Ethovision XT10 (Noldus Information Technology, Toronto, Canada).

Novel object recognition test

The novel object recognition test was conducted in a transparent acrylic chamber (31 x 31 cm), and the objects used during the task were different in shape, color, size, and material. On the first day, mice were habituated to the empty arena for two 10-minute sessions, 6 hours apart. On the second day, mice were put back in the arena for 10 minutes, and two identical objects were presented. After 6 hours, one of the familiar objects was replaced with a novel object before allowing the mouse to explore the arena and objects for 10 minutes. The total time spent exploring each of the two objects (novel and familiar) was recorded and analyzed using Ethovision XT10

(Noldus Information Technology, Toronto, Canada). Object exploration was defined as the orientation of the nose to the object at a distance of less than 2 cm [42, 43]. The discrimination index was calculated as the percentage of time spent investigating the novel object *vs.* the total object exploration time: discrimination index = novel object exploration time/(novel object exploration time + familiar object exploration time) ×100. All experiments were scored by scientists blind to the experimental groups. The objects were cleaned with 70% ethanol after each trial.

Displaced object test

The displaced object test was conducted in a transparent acrylic chamber (44 x 44 cm) with a black and white striped pattern on one wall. On the first day, mice were habituated to the empty chamber for two 10-minute sessions, 6 hours apart. On the second day, the mice were exposed to identical objects for 10 min during the acquisition phase. Six hours later, one of the objects was moved, and the mouse was allowed to explore for 10 minutes. The total time spent exploring each object was recorded and analyzed using Ethovision XT10 (Noldus Information Technology, Toronto, Canada). Exploration was considered as any head orientation and sniffing < 1.0 cm from the object or deliberate contact with the object [42, 44]. The discrimination index was calculated as the percentage of time spent investigating the displaced object *vs*. total object exploration time: discrimination index = displaced object exploration time/ (displaced object exploration time + non-displaced object exploration time) × 100. All experiments were video recorded and scored by scientists blind to the experimental groups.

Sociability Test

The sociability test was conducted in a rectangular, three-chambered apparatus (56 inch × 10 inch × 12 inch). The dividing walls among the three chambers were made from clear Plexiglas, with an open doorway to allow access across chambers. One day prior to the test, animals were

given 10 minutes to acclimatize to the apparatus where they moved freely across the three empty chambers. On the experimental day, all three compartments were isolated. Animals were placed in the middle chamber for 5 minutes. Next, a control mouse (i.e. stranger 1, S1) was placed inside an upside-down wire cup that served as a temporary cage located in one of the side chambers. The other side chamber contained an empty wire cup. At the start of the test, the doors between compartments were opened to allow the test animal to freely explore the three chambers for 10 minutes. In the final phase of the experiment, a second control mouse (stranger 2, S2) was placed inside the previously empty wire cup in the other side chamber. Again, the test mouse was observed while exploring all three chambers for another 10 minutes. All behaviour was recorded and analyzed using Ethovision XT10 (Noldus Information Technology, Toronto, Canada).

Immunohistochemistry

Mouse brains were fixed in 4% paraformaldehyde overnight, then put in 30% sucrose. After dehydration, frozen coronal sections of 25-μm thickness were cut using cryostat for immunofluorescence staining. All sections were permeabilized with 0.3% Triton X-100 in PBS for 30 minutes, and blocked with 2% bovine serum albumin in PBS at room temperature for 1 hour. Sections were incubated with anti-Iba1 (1:200, Novus Biologicals, catalog #NB100-1028), anti-PSD95 (1:300, SYSY, catalog #124008 for colocalization with Iba1), anti-C1q (1:200, Abcam, catalog #ab182451), and anti-PSD95 (1:200, SYSY, catalog #124011 for colocalization with C1q), anti-NeuN (1:200, Millipore, catalog #MAB377), anti-Ctip2 (1:50, Abcam, catalog #ab18465) for colocalization with anti-TAT (1:300, Abcam, catalog #ab43014) at 4°C overnight. Secondary antibody was probed for 1.5 hours at room temperature.

For 2D analysis of Iba1 and PSD95 colocalization, images were acquired using an Olympus FluoView FV1200 confocal microscope at ×60 magnification with 1 μm z-steps. To

quantify fraction of Iba1 overlapping PSD95, signals outside of the microglia were filtered from the image by Threshold Color in ImageJ, then analyzed by M1 & M2 coefficients using the JACoP plugin in ImageJ.

For 3D analysis of Iba1 and PSD95 colocalization, images were captured with a Zeiss LSM 880 Super Resolution confocal microscope at ×63 magnification using 0.2 μm z-steps, then structured illumination processing by Zen software (Zeiss). 3D-surface rendered images were created by Imaris software (Bitplane 9.8). To calculate the engulfed PSD95 within microglia, signals outside of the microglia were processed by using the mask function in Imaris. The engulfment metric was calculated as the total volume of masked PSD95 volume (μm3)/volume of microglia (μm^3).

For analysis of C1q and PSD95 colocalization, images were acquired using an Olympus FluoView FV1200 confocal microscope at ×63 magnification with 2 μm z-steps. Colocalizations were quantified using ImageJ software as previously described [45, 46] in four random regions of interest (ROIs) in the cortex.

General statistical analysis

Data were analyzed by two-tailed unpaired t-test, or a one-, or two-way analysis of variance (ANOVA) followed by *post hoc* Tukey's test as specified in the figure legend (GraphPad Prism 9.0, GraphPad Software, CA, USA). Data satisfied parametric assumptions of equal variance and normality, and no data points were excluded as outliers. All data were expressed as mean ± standard error of mean (S.E.M.). The significance levels of $p< 0.05$, $p<0.01$, or $p<0.001$ were used for all analyses.

Results

EF1α-Mdm2, EF1α-TRIM3 complexes are increased in the brain of *Fmr1* KO mice.

To identify potential EF1α-associated protein complexes involved in the pathophysiology of FXS**,** we used EF1α antibody to co-immunoprecipitate proteins from whole brain tissue of *Fmr1* KO mice. The precipitated proteins were analyzed with mass spectrometry, which identified Mdm2 and TRIM3 as EF1α interacting proteins. We focused on Mdm2 and TRIM3 because both are members of the E3 ubiquitin ligase family previously implicated in the pathology of neurodevelopmental disorders such as autism spectrum disorder (ASD) and FXS [23, 29, 42]. Mdm2 has been shown to ubiquitinate PSD-95, and this process is an important part of the molecular regulation of dendritic spine pruning by microglia [23].

We first confirmed the existence of the EF1α-Mdm2 and EF1α-TRIM3 protein complexes in normal wild-type (C57BL/6) mouse brain with co-immunoprecipitation. As depicted in **Fig. 1A**, primary antibodies against Mdm2 co-immunoprecipitated EF1α (top panel), and *vice versa* (bottom panel), in mouse brain protein extracts, confirming the existence of the EF1α-Mdm2 complex in mouse brain. The same experiment with *Fmr1* KO mice showed significantly higher levels of EF1α-Mdm2 complex compared to wild-type control mice ($p < 0.05$, $t_4 = 2.862$) (**Fig. 1B-C**). The amount of directly immunoprecipitated EF1α was not significantly different between wild-type and *Fmr1* KO mice. Using the same strategy, we also confirmed that TRIM3 formed a complex with EF1α in mouse brain (**Fig. 1D**), and that the EF1α-TRIM3 complex significantly increased in *Fmr1* KO mice compared to wild-type controls ($p < 0.05$, $t_4 = 3.053$) (**Fig. 1E-F**).

We then measured the ratio of the amount of Mdm2-EF1α and EF1α-TRIM3 complexes to the total expression level of EF1α. As shown in **Fig. 1G-J**, about 15.48% ± 0.94% of EF1α forms complex with Mdm2 and 2.25% ± 0.15% forms a complex with TRIM3 in wild-type mice. In

Fmr1 KO mice, about 20.31% ± 0.92% of the EF1α forms a complex with Mdm2 and 3.30% ± 0.09% with TRIM3. Evidently, there is a much greater quantity of Mdm2-EF1α complex than EF1α-TRIM3 complex in both wild-type and *Fmr1* KO mice.

Development of an interfering peptide (TAT-EF1α) that disrupts the EF1α-Mdm2 and EF1α-TRIM3 complexes.

If increased amounts of the EF1α-Mdm2 and EF1α-TRIM3 protein complexes in *Fmr1* KO mouse brain are part of the pathway leading to abnormal dendritic morphology and behaviour, disruption of these complexes should rescue these deficits. To develop a peptide capable of disrupting EF1α-Mdm2 and EF1α-TRIM3 complexes, we first sought to identify the protein domains necessary for these proteins to bind each other. As in our previous work, we accomplished this by a series of affinity purification assays with GST fusion proteins containing various fragments of EF1α. As shown in **Fig. 2A**, GST-EF1α1 (M1-P241) precipitated Mdm2 from solubilized mouse brain tissue, indicating that Mdm2 can interact with EF1α *via* the EF1α-1 fragment. Using the same strategy, we examined parts of the EF1α1 region (**Supplementary Figure 1**) and concluded that the EF1α-1-2-2 (L77-D91: LWKFETSKYYVTIID) fragment contains the region that specifically interacts with Mdm2 (**Fig. 2B-C**). We synthesized a peptide named TAT-EF1α based on the amino acid sequence of this fragment. We also fused this peptide with the cell-membrane transduction domain of the human immunodeficiency virus-type 1 TAT protein to facilitate transport across target cell membranes [35, 36]. If the EF1α-1-2-2 region is essential for EF1α-Mdm2 binding, TAT-EF1α should disrupt the EF1α-Mdm2 complex by competing with EF1α for Mdm2. As expected, TAT-EF1α but not the control TAT peptide reduced EF1α-Mdm2 complex levels in mouse brain extracts (**Fig. 2D**).

We used the same strategy to identify the region of EF1α that is necessary for EF1α-TRIM3 complex formation and surprisingly found that TRIM3 binds to the same region as Mdm2, EF1α-1-2-2 (L77-D91) (**Fig. 2E-G**). Consistent with this finding, TAT-EF1α, but not the control TAT peptide, reduced EF1α-TRIM3 complex levels in mouse brain extracts (**Fig. 2H**). Thus, we conclude that the EF1α-1-2-2 region is necessary for both EF1α-Mdm2 complex and EF1α-TRIM3 complex formation, and that the TAT-EF1α peptide disrupts both the EF1α-Mdm2 and EF1α-TRIM3 complexes.

To confirm that TAT-EF1α disrupts these two protein complexes, EF1α-Mdm2 and EF1α-TRIM3, we performed *i.p.* injections of TAT-EF1α or control peptide (TAT) in *Fmr1* KO mice from P14 to P20, a period of active spine pruning. In *Fmr1* KO mice, the higher levels of both EF1α-Mdm2 (**Fig. 2I-J**) and EF1α-TRIM3 (**Fig. 2K-L**) protein complexes were significantly reduced by TAT-EF1α peptide (EF1α-Mdm2: $p < 0.0001$, $F_{3,8} = 0.2250$; EF1α-TRIM3: $p < 0.001$, $F_{2,9} = 0.8476$). In summary, we discovered that the EF1α-1-2-2 region is responsible for binding to Mdm2 and TRIM3, and verified that our synthetic peptide TAT-EF1α disrupts the EF1α-Mdm2 and EF1α-TRIM3 complexes *in vivo*.

TAT-EF1α restores dendritic spine plasticity in *Fmr1* KO mice

Previous studies have shown elevated dendritic spine density in *Fmr1* KO mice [47-50]. We hypothesized that TAT-EF1α would reduce dendritic spine density to wild-type levels in *Fmr1* KO mice. We first verified the brain penetration of TAT-EF1α peptide 1 h post i.p. injection (3 nmol/g) in *Fmr1* KO mice. We used antibodies against TAT to visualize TAT peptide in the brain, and co-stained for either NeuN or Ctip2 to detect neurons and layer 5 neurons, respectively. We found 41.36% [95% CI: 37.8-44.9] of cortical $NeuN^+$ neurons contained TAT staining and 41.40% [95% CI: 37.7-45.1] of $Ctip2^+$ L5 neurons contained TAT staining 1 h after TAT-EF1α injection

(**Supplementary Figure 2A-D**). To test the effects of TAT-EF1α peptide on dendritic spine density, we injected *Fmr1* KO mice with TAT-EF1α, control TAT peptide or saline (*i.p.*) from P14 to P20 (3 nmol/g per day) (**Supplementary Figure 2E**). As shown in **Fig. 3A-B**, dendritic spine density in frontal cortex visualized by Golgi-Cox staining was significantly higher in brain slices from *Fmr1* KO mice compared to WT mice. TAT-EF1α peptide treatment decreased dendritic spine density in *Fmr1* KO mice to WT levels. This rescue of dendritic spine density is important because dendritic spines are the main site of excitatory synaptic transmission in the brain. However, Golgi staining provides only a single cross-sectional *post mortem* sampling of dendritic spine density. Hence, we also used live *in vivo* microscopy to visualize dynamic changes in dendritic spine morphology and number.

Impaired structural plasticity of dendritic spines has been reported in the cerebral cortex of *Fmr1* KO mice [51-54]. To further investigate the effects of TAT-EF1α treatment on dendritic spine development, we crossed *Fmr1* KO mice with *Thy1*-YFP mice expressing yellow fluorescent protein (YFP) in layer 5 pyramidal neurons, and visualized postsynaptic dendritic spines in the frontal association cortex of living mice with transcranial two-photon microscopy (**Fig. 3C-D**). Consistent with previous studies [51-54], we found that *Fmr1* KO mice had a delayed stabilization of dendritic spine dynamics. The rates of dendritic spine elimination and formation over 2 days (**Fig. 3E)** or 10 days (**Fig. 3F)** in *Fmr1* KO mice were significantly higher than those in WT mice. From postnatal day (P) 21 to P23 in WT mice, 17.0 ± 0.9% of dendritic spines were eliminated and 11.0 ± 0.6% were formed. In contrast, for *Fmr1* KO mice, 22.9 ± 1.0% and 19.3 ± 1.0% of dendritic spines were eliminated and formed, respectively. *Fmr1* KO mice pre-treated with TAT-EF1α showed a significant decrease in spine elimination and formation compared to *Fmr1* KO mice injected with saline. The TAT control peptide had no effect on spine dynamics in *Fmr1* KO mice.

Additionally, we observed no significant difference in cortical spine density on P31 between WT mice and *Fmr1* KO mice pre-treated with TAT-EF1α (**Fig. 3G**). Together, these experiments indicate that dendritic spine plasticity is impaired in the frontal cortex of developing *Fmr1* KO mice. TAT-EF1α treatment during the early postnatal period rescues spine plasticity and density in *Fmr1* KO mice, further supporting therapeutic potential in FXS.

TAT-EF1α restores behavioural deficits in *Fmr1* KO mice

We have shown the TAT-EF1α peptide is able to rescue abnormalities in spine density and plasticity in *Fmr1* KO mice. We then sought to determine whether behavioural deficits in *Fmr1* KO mice would also be rescued by TAT-EF1α peptide treatment. We examined common animal behaviours relevant to FXS symptoms in humans: anxiety, learning and memory deficits, and sociability [42, 55]. *Fmr1* KO mice were injected (*i.p.*) with either TAT-EF1α, control peptide (TAT) or saline from P14 to P20 for all behavioural tests, and immunoprecipitation confirmed that TAT-EF1α disrupted the EF1α-Mdm2 and EF1α-TRIM3 complexes (**Fig. 2I-L)**. All behavioural analyses were carried out at 8-weeks of age (**Supplementary Figure 2F**). Anxiety-like behaviour was assessed with the elevated plus-maze, and we found that *Fmr1* KO mice injected with TAT-EF1α had less anxiety-like behaviour ($p < 0.0001$, $F_{3, 20} = 4.546$) (**Fig. 3H**). We also examined whether TAT-EF1α could rescue learning and memory abnormalities using the displaced object and novel object tests. TAT-EF1α treatment rescued deficits in both tests in *Fmr1* KO mice (**Fig. 3I-J**) (Fig. 4B: $p < 0.01$, $F_{3, 22} = 1.517$; Fig. 4C: $p < 0.001$, $F_{3, 22} = 0.5517$). Social interaction was tested using Crawley's three-chamber test, in which saline-injected *Fmr1* KO mice showed an abnormal lack of interest in a novel mouse (S2) over a familiar mouse (S1). TAT-EF1α rescued this abnormal social behaviour in *Fmr1* KO mice (**Fig. 3K**).

TAT-EF1α rescues impaired synaptic pruning in *Fmr1* KO mice

Previous studies have reported there is reduced microglial synaptic pruning in *Fmr1* KO mouse brains [8]. We confirmed increased spine density in *Fmr1* KO mice, which could arise from impaired synaptic pruning. To test this hypothesized cellular mechanism, we performed immunohistochemistry with antibodies against Iba1 (ionized calcium-binding adapter molecule 1), which is encoded by a major histocompatibility complex class III gene, and often used as an immunohistochemical marker for microglia [56]. Consistent with previous reports, we observed significantly decreased co-localization of Iba1 and PSD-95 in the *Fmr1* KO mouse cortex, suggesting reduced microglia-mediated synaptic pruning. TAT-EF1α peptide normalizes the co-localization of Iba1 and PSD-95 in *Fmr1* KO mice to that of WT mice (**Fig. 4A-B**).

To directly visualize synaptic engulfment by microglia, we performed super-resolution structured illumination microscopy (SIM) with a Leica LSM 880 Elyra machine as previously described [57]. To observe the phagocytosis of synaptic proteins, we stained with fluorescent antibodies against the synaptic protein PSD-95 and the microglial marker Iba1 [58]. We found that $Iba1^+$ microglia have fewer $PSD95^+$ puncta in *Fmr1 KO* mice compared to WT mice. To visualize the engulfed $PSD95^+$ puncta within microglia, any fluorescence that is outside of the microglia was subtracted from the image using Imaris software [57] (**Fig. 4C-D**).

The molecular regulation of synaptic pruning by microglia is complex [59, 60], and includes components of the complement cascade [46, 60-63]. The initial signal from neurons to microglia for synaptic pruning begins with C1q, which forms a complex with PSD-95 that tags synapses for elimination [64, 65]. In *Fmr1* KO mice, we observed an increased Mdm2 interaction with EF1α that may decrease Mdm2 coupling with PSD-95 ($p < 0.001$, $F_{3, 8} = 0.5327$) (**Fig. 4E-F**). Since Mdm2 couples to PSD-95 and increases PSD-95 ubiquitination, a decrease in the Mdm2-PSD-95 complex should lead to less PSD-95 ubiquitination. As shown in **Fig. 4G-H**, the amount of Ub-PSD-95 is

significantly decreased in *Fmr1* KO mice, and injection of TAT-EF1α normalizes Ub-PSD-95 levels to that of WT mice ($p < 0.0001$, $F_{3, 8} = 0.8914$).

The binding of C1q with PSD-95 initiates synapse elimination, so we then investigated whether C1q-PSD-95 complex levels are altered in *Fmr1* KO mice. As shown in **Fig. 4I-J**, confocal microscopy revealed less C1q-PSD-95 co-localization in *Fmr1* KO mice compared to WT mice. Injection of TAT-EF1α into *Fmr1* KO mice restored C1q-PSD-95 co-localization to the normal level seen in WT mice, but the control peptide TAT had no effect. One possible confound that could lower the level of C1q-PSD-95 co-localization in *Fmr1* KO mice is the degree to which PSD-95 is ubiquitinated. Since we observed decreased Ub-PSD-95 levels, we hypothesized that C1q preferentially complexes with Ub-PSD-95 over non-ubiquitinated PSD-95. Consistent with this hypothesis, the level of C1q-PSD-95 complex is significantly lower in protein extracted from brain slices treated with the Mdm2 inhibitor Nutlin-3 (5 μM, 1 hour) vs. saline control ($p < 0.01$, $t_6 = 4.603$) (**Fig. 4K-L**). These data suggest that TAT-EF1α peptide regulates synaptic pruning and spine plasticity through Ub-PSD-95, which is a molecular tag for spines to be eliminated.

TAT-EF1α facilitates C3 activation in *Fmr1* KO mice

The role of the classical complement cascade in synaptic pruning has only recently been demonstrated. Microglial cells recognize activated C3 bound to synapses targeted for elimination, triggering their engulfment. An interesting connection to our results above is that a previous study identified C3 as a potential TRIM3 substrate [66], but not PSD-95 [29]. We showed increased EF1α-TRIM3 complex in *Fmr1* KO mice, suggesting that excessive EF1α in *Fmr1* KO might bind and sequester TRIM3, thereby decreasing TRIM3-C3 interaction and C3 activation.

We confirmed our hypothesis by observing decreased TRIM3-C3 complex in *Fmr1* KO mice ($p < 0.05$, $t_4 = 3.036$) (**Fig. 5A-B**), which was rescued by TAT-EF1α peptide injection from

P14–P20 ($p < 0.01$, $F_{2, 9} = 1.015$) (**Fig. 5C-D**). We then examined whether TAT-EF1α released TRIM3 from EF1α sequestration, allowing TRIM3 to facilitate C3 activation. As shown in **Fig. 5E-G**, C3b is significantly decreased in *Fmr1* KO mice while C3 is increased, but TAT-EF1α injection normalizes both C3b and C3 levels in *Fmr1* KO mice (**Fig. 5F**: $p < 0.01$, $F_{3, 8} = 0.3286$; **Fig. 5G**: $p < 0.001$, $F_{3, 8} = 0.459$). These data suggest that TAT-EF1α facilitates C3 activation. Since TAT-EF1α disrupts both the EF1α-Mdm2 and EF1α-TRIM3 complexes, we sought to demonstrate that TRIM3 is necessary for C3b upregulation by knocking-down TRIM3 with siRNA. As shown in **Fig 5H-K**, Trim3 siRNA successfully reduced TRIM3 levels ($p < 0.05$, $t_4 = 4.204$) (**Fig. 5H bottom**) and decreased C3b ($p < 0.01$, $t_4 = 6.375$) without significantly altering total expression of C3. These data suggest that TRIM3 is necessary for TAT-EF1α induced C3 activation.

Discussion

The results presented above demonstrate that EF1α interacts with and forms a protein complex with Mdm2 and TRIM3, which both bind to EF1α at the same region. By deciphering the amino acid sequence in this binding region, we were able to create a small peptide, TAT-EF1α, that can disrupt both protein complexes. Both the EF1α-Mdm2 and EF1α-TRIM3 complexes are found at higher levels in the *Fmr1* KO mouse, which has excess spines on neuronal dendrites, and behavioural abnormalities relevant to FXS in humans: increased anxiety, impaired object memory and decreased social interaction. The TAT-EF1α peptide rescues these broad phenotypes, and also normalizes a series of molecular abnormalities in the *Fmr1* KO mouse that illuminate the mechanism for impaired dendritic spine dynamics.

Dendritic spines are the post-synaptic structure that receives inputs from upstream neurons, and changes in dendritic spines are a visible structural manifestation of synaptic plasticity. Spine density also follows a stereotypical developmental trajectory, with a peak in early childhood, pruning during adolescence and stability during adulthood until decline in senescence [67]. Pruning of dendritic spines is the result of a complex cellular process that is regulated at many levels. Here we report new insights into some of the molecular mechanisms that control dendritic spine dynamics, with specific relevance to FXS but also more broadly for understanding neurodevelopmental disorders.

Our hypothetical model is shown in **Fig. 6**. Conditions favouring synapse elimination in control mice are shown in the top panel. Briefly, Mdm2 is functioning here as a ubiquitin E3 ligase, binding and ubiquitinating PSD-95 in the dendritic spine, which complexes further with Pchd10 and the proteosome to degrade that spine. At the same time, ubiquitinated PSD-95 (Ub-PSD-95) binds C1q, the initial component of the complement cascade that signals through C3 and the CR3 receptor on microglia to trigger phagocytosis. TRIM3 also binds to C3 and contributes to activation of the complement cascade, acting synergistically with the Ub-PSD-95-C1q complex to drive phagocytosis and degradation of the dendritic spine. Conversely, the conditions that inhibit synaptic pruning in *Fmr1* KO mice and stabilize dendritic spines are shown in the bottom panel. Loss of FMRP removes translational suppression of eukaryotic translation elongation factor 1-α (*EF1α*). The increased amounts of EF1α bind to and sequester both Mdm2 and TRIM3, preventing them from binding with PSD-95 or C3, thus inhibiting spine degradation and phagocytosis by microglia [22, 23, 68].

There are a number of important limitations to discuss. The first is that we focused on a specific molecular cascade surrounding the EF1α protein because it is significantly increased by

the lack of FMRP protein in FXS. This does not diminish the importance of many other pathways regulating synaptic structure and plasticity. Our focus was also on the pruning of synapses rather than the genesis and maintenance of spines, which is of course equally important in the eventual equilibrium that is visible through the microscope. Our traditional histology data obtained with Golgi staining confirm elevated spine density in *Fmr1* KO mice from a single cross-sectional *post mortem* examination. *In vivo* transcranial two-photon microscopy reveals a more complex picture, with higher formation and elimination of dendritic spines in the *Fmr1* KO mouse between P21-23. Our hypothetical model provides a framework for connecting the varied abnormal protein interactions that we studied in this paper. We were selective in the choice of protein interactions to study and were guided by previous data suggesting relevance to synaptic pruning, but these specific interactions are not necessarily as important for regulating spine formation.

An important question arising from our data is the relationship between the EF1α-Mdm2 and EF1α-TRIM3 protein complexes. In **Fig. 1G-I**, it is apparent that under normal conditions, the EF1α-Mdm2 complex occupies ~15% of total EF1α, while only ~2% of EF1α forms complex with TRIM3. Because EF1α interacts with both Mdm2 and TRIM3 at the same site, it is likely that the two complexes are in competition, similar to two different ligands competitively binding to the same site on a receptor. Like receptor-ligand interactions, these protein interactions are likely to be transient, with binding and dissociation events occurring simultaneously that result in an equilibrium. One could hypothesize that Mdm2 has higher affinity for EF1α than TRIM3, but our data do not provide direct information about this possibility. A future experiment using BRET/FRET could help to determine relative binding affinity of Mdm2 and TRIM3 for EF1α.

It is theoretically possible that Mdm2 and TRIM3 bind to different parts of the EF1α binding domain, and that our GST fusion protein fragments were too large to resolve this

separation. If Mdm2 and TRIM3 have distinct binding regions on EF1α, this could enable the three proteins to form a triple complex, and this possibility could be investigated with X-ray crystallography to illuminate the bound configuration of these proteins. Targeted mutations to alter the binding regions of the three proteins could be an alternative strategy to investigate the possibility of a triple protein complex. Nevertheless, in our hypothetical model, the critical event in the pathophysiology of disturbed spine regulation in *Fmr1* KO mice is increased EF1α protein that sequesters both Mdm2 and TRIM3. The EF1α-Mdm2 and EF1α-TRIM3 protein complexes have related but distinct functions in promoting the phagocytosis and degradation of spines, and act synergistically on different parts of the cellular pruning pathway.

We observed decreased levels of both Ub-PSD-95 and C1q-PSD-95 complex in *Fmr1* KO mice. The Mdm2 inhibitor Nutlin-3 (5 μM, 1 hour) also decreased Ub-PSD-95 levels, which is consistent with what we observed in *Fmr1* KO mice, in which higher levels of EF1α lowers Mdm2 through sequestration in the EF1α-Mdm2 complex. It is likely that C1q has higher affinity for Ub-PSD-95 than non-ubiquinated PSD-95, since this would lead to greater activation of the complement cascade through C3b and beyond. However, we did not directly test this possibility, and this could be the subject of future experiments.

Current treatments for FXS and ASD only address symptoms and their efficacy is limited, as would be expected for treatments that do not modify the underlying cause, nor alter the abnormal synaptic development in these disorders. An obvious but technically challenging way to treat the underlying cause of genetic disorders like FXS is with gene therapy [69]. Molecular biology tools used routinely in the lab and in model organisms could potentially be translated into clinical treatments to express exogeneous genes, increase the expression of deficient proteins such as FMRP, or supressing the expression of deleterious mutations [70]. Recombinant adeno-associated

viral vectors have been used successfully in neonates to correct spinal muscular atrophy, which is caused by a deficiency in the protein encoded by the survival motor neuron 1 (SMN1) gene [71]. Without diminishing the significance of these types of advances in gene therapy for brain disorders, there remain significant obstacles and challenges. Viral vectors have the potential for immunological side effects, and while they have high specificity for the target DNA sequence, calibration of gene dosage and modulation of expression is not trivial. The regulation of gene expression remains to be fully deciphered [72], and this broad biological issue is of particular importance when attempting to rectify aberrant gene expression to the proper physiological level in a particular region of the brain during a critical period of development.

A complementary and alternative strategy for the treatment of developmental brain disorders with genetic origins could be to disrupt abnormally elevated protein-protein interactions. In our previous work we identified protein complexes, often involving neurotransmitter receptors, that are elevated in a variety of adult brain disorders such as schizophrenia, PTSD and multiple sclerosis, and that could be normalized with a therapeutic interfering peptide [35, 37, 73]. Our current work is novel in being relevant to a developmental brain disorder, which offers the possibility of early intervention before the disease process has consolidated the pathology. Here we have identified the potential of the EF1α-Mdm2 and EF1α-TRIM3 interactions as therapeutic targets for early intervention in FXS and possibly for other forms of ASD with dendritic spine pruning deficits. TAT-EF1α could be given during childhood or adolescence to potentially rectify spine pruning. This approach could revolutionize clinical management of these disorders by correcting aberrant brain development during a critical window, preventing disease pathology rather than treating the results. Another advantage of our therapeutic peptide would be that a time-limited burst of treatment could be potentially curative, unlike the chronic medication treatments currently

required for almost all neuropsychiatric disorders. Of course, much more work is required to realize this potential treatment, but the data presented here are the first step: identifying a novel molecular treatment target that could correct the abnormal neurodevelopmental trajectory in a genetic syndrome causing significant morbidity and intellectual disability.

Acknowledgement

The study was supported by Canadian Institute of Health Research (F.L.), and Centre for Addiction and Mental Health, Department of Psychiatry, University of Toronto (F.L.). Dr. Fang Liu holds the Tapscott Chair in Schizophrenia studies.

Author Contribution

F.L. oversaw and designed the framework of the research. P.S. designed and performed biochemistry experiments, Golgi-Cox staining, behavioural tests, and analyzed data with help from F.H.F.L. (spine density) and T.K.Y.L. (behavioural tests). K.C., L.H., H.Z., and G.Y. designed, conducted and analyzed the data from *in vivo* transcranial two-photon imaging. S.Y., L.W., and A.J. performed the immunohistochemical analysis. P.S., S.Y., L.H., H.Z., L.W., and A.J. prepared the figures. F.L., P.S., S.Y., L.W., L.H., H.Z., J.S., G.Y., and A.H.C.W. wrote the manuscript.

Data Availability

The authors declare that data supporting the findings of this study are availale from the corresponding author upon request.

Conflict of interests

The authors declare no competing financial interests.

Supplementary information is available at Molecular Psychiatry's website.

REFERENCES

1. Hagerman RJ, Polussa J. Treatment of the psychiatric problems associated with fragile X syndrome. *Current opinion in psychiatry* 2015; **28**(2)**:** 107-112.

2. Wang T, Bray SM, Warren ST. New perspectives on the biology of fragile X syndrome. *Current opinion in genetics & development* 2012; **22**(3)**:** 256-263.

3. Lozano R, Azarang A, Wilaisakditipakorn T, Hagerman RJ. Fragile X syndrome: A review of clinical management. *Intractable Rare Dis Res* 2016; **5**(3)**:** 145-157.

4. Aishworiya R, Valica T, Hagerman R, Restrepo B. An Update on Psychopharmacological Treatment of Autism Spectrum Disorder. *Neurotherapeutics* 2022; **19**(1)**:** 248-262.

5. Tranfaglia MR. The psychiatric presentation of fragile x: evolution of the diagnosis and treatment of the psychiatric comorbidities of fragile X syndrome. *Dev Neurosci* 2011; **33**(5)**:** 337-348.

6. Irwin SA, Galvez R, Greenough WT. Dendritic spine structural anomalies in fragile-X mental retardation syndrome. *Cerebral cortex (New York, NY : 1991)* 2000; **10**(10)**:** 1038-1044.

7. Bagni C, Zukin RS. A Synaptic Perspective of Fragile X Syndrome and Autism Spectrum Disorders. *Neuron* 2019; **101**(6)**:** 1070-1088.

8. Jawaid S, Kidd GJ, Wang J, Swetlik C, Dutta R, Trapp BD. Alterations in CA1 hippocampal synapses in a mouse model of fragile X syndrome. *Glia* 2018; **66**(4)**:** 789-800.

9. Uzunova G, Pallanti S, Hollander E. Excitatory/inhibitory imbalance in autism spectrum disorders: Implications for interventions and therapeutics. *The world journal of biological psychiatry : the official journal of the World Federation of Societies of Biological Psychiatry* 2016; **17**(3)**:** 174-186.

10. Berry KP, Nedivi E. Spine Dynamics: Are They All the Same? *Neuron* 2017; **96**(1)**:** 43-55.

11. Darnell JC, Van Driesche SJ, Zhang C, Hung KY, Mele A, Fraser CE *et al.* FMRP stalls ribosomal translocation on mRNAs linked to synaptic function and autism. *Cell* 2011; **146**(2)**:** 247-261.

12. Ascano M, Jr., Mukherjee N, Bandaru P, Miller JB, Nusbaum JD, Corcoran DL *et al.* FMRP targets distinct mRNA sequence elements to regulate protein expression. *Nature* 2012; **492**(7429)**:** 382-386.

13. Sung YJ, Dolzhanskaya N, Nolin SL, Brown T, Currie JR, Denman RB. The fragile X mental retardation protein FMRP binds elongation factor 1A mRNA and negatively regulates its translation in vivo. *The Journal of biological chemistry* 2003; **278**(18)**:** 15669-15678.

14. Riis B, Rattan SI, Clark BF, Merrick WC. Eukaryotic protein elongation factors. *Trends in biochemical sciences* 1990; **15**(11)**:** 420-424.

15. Negrutskii BS, El'skaya AV. Eukaryotic translation elongation factor 1 alpha: structure, expression, functions, and possible role in aminoacyl-tRNA channeling. *Progress in nucleic acid research and molecular biology* 1998; **60:** 47-78.

16. Huang F, Chotiner JK, Steward O. The mRNA for elongation factor 1alpha is localized in dendrites and translated in response to treatments that induce long-term depression. *The Journal of neuroscience : the official journal of the Society for Neuroscience* 2005; **25**(31)**:** 7199-7209.

17. Hamrita B, Nasr HB, Hammann P, Kuhn L, Guillier CL, Chaieb A *et al.* An elongation factor-like protein (EF-Tu) elicits a humoral response in infiltrating ductal breast carcinomas: an immunoproteomics investigation. *Clin Biochem* 2011; **44**(13)**:** 1097-1104.

18. Chang JS, Seok H, Kwon TK, Min DS, Ahn BH, Lee YH *et al.* Interaction of elongation factor-1alpha and pleckstrin homology domain of phospholipase C-gamma 1 with activating its activity. *The Journal of biological chemistry* 2002; **277**(22)**:** 19697-19702.

19. Yang J, Fuller PJ, Morgan J, Shibata H, McDonnell DP, Clyne CD *et al.* Use of phage display to identify novel mineralocorticoid receptor-interacting proteins. *Mol Endocrinol* 2014; **28**(9)**:** 1571-1584.

20. Vera M, Pani B, Griffiths LA, Muchardt C, Abbott CM, Singer RH *et al.* The translation elongation factor eEF1A1 couples transcription to translation during heat shock response. *Elife* 2014; **3:** e03164.

21. Frum R, Busby SA, Ramamoorthy M, Deb S, Shabanowitz J, Hunt DF *et al.* HDM2-binding partners: interaction with translation elongation factor EF1alpha. *Journal of proteome research* 2007; **6**(4)**:** 1410-1417.

22. Tsai NP, Wilkerson JR, Guo W, Huber KM. FMRP-dependent Mdm2 dephosphorylation is required for MEF2-induced synapse elimination. *Human molecular genetics* 2017; **26**(2)**:** 293-304.

23. Tsai NP, Wilkerson JR, Guo W, Maksimova MA, DeMartino GN, Cowan CW *et al.* Multiple autism-linked genes mediate synapse elimination via proteasomal degradation of a synaptic scaffold PSD-95. *Cell* 2012; **151**(7)**:** 1581-1594.

24. Tocchini C, Ciosk R. TRIM-NHL proteins in development and disease. *Semin Cell Dev Biol* 2015; **47-48:** 52-59.

25. Micale L, Chaignat E, Fusco C, Reymond A, Merla G. The tripartite motif: structure and function. *Adv Exp Med Biol* 2012; **770:** 11-25.

26. El-Husseini AE, Fretier P, Vincent SR. Cloning and characterization of a gene (RNF22) encoding a novel brain expressed ring finger protein (BERP) that maps to human chromosome 11p15.5. *Genomics* 2001; **71**(3)**:** 363-367.

27. Liu Y, Raheja R, Yeh N, Ciznadija D, Pedraza AM, Ozawa T *et al.* TRIM3, a tumor suppressor linked to regulation of p21(Waf1/Cip1.). *Oncogene* 2014; **33**(3)**:** 308-315.

28. Boulay JL, Stiefel U, Taylor E, Dolder B, Merlo A, Hirth F. Loss of heterozygosity of TRIM3 in malignant gliomas. *BMC Cancer* 2009; **9:** 71.

29. Hung AY, Sung CC, Brito IL, Sheng M. Degradation of postsynaptic scaffold GKAP and regulation of dendritic spine morphology by the TRIM3 ubiquitin ligase in rat hippocampal neurons. *PLoS One* 2010; **5**(3)**:** e9842.

30. Martins-de-Souza D, Gattaz WF, Schmitt A, Maccarrone G, Hunyadi-Gulyás E, Eberlin MN *et al.* Proteomic analysis of dorsolateral prefrontal cortex indicates the involvement of cytoskeleton, oligodendrocyte, energy metabolism and new potential markers in schizophrenia. *J Psychiatr Res* 2009; **43**(11)**:** 978-986.

31. Janeway CA Jr TP, Walport M, et al. The complement system and innate immunity. *Immunobiology: The Immune System in Health and Disease*, 5th edition edn2001.

32. Fu H, Liu B, Frost JL, Hong S, Jin M, Ostaszewski B *et al.* Complement component C3 and complement receptor type 3 contribute to the phagocytosis and clearance of fibrillar Aβ by microglia. *Glia* 2012; **60**(6)**:** 993-1003.

33. Ramaglia V, Hughes TR, Donev RM, Ruseva MM, Wu X, Huitinga I *et al.* C3-dependent mechanism of microglial priming relevant to multiple sclerosis. *Proc Natl Acad Sci U S A* 2012; **109**(3)**:** 965-970.

34. Zang T, Maksimova MA, Cowan CW, Bassel-Duby R, Olson EN, Huber KM. Postsynaptic FMRP bidirectionally regulates excitatory synapses as a function of developmental age and MEF2 activity. *Molecular and cellular neurosciences* 2013; **56:** 39-49.

35. Su P, Li S, Chen S, Lipina TV, Wang M, Lai TK *et al.* A dopamine D2 receptor-DISC1 protein complex may contribute to antipsychotic-like effects. *Neuron* 2014; **84**(6)**:** 1302-1316.

36. Pei L, Li S, Wang M, Diwan M, Anisman H, Fletcher PJ *et al.* Uncoupling the dopamine D1-D2 receptor complex exerts antidepressant-like effects. *Nat Med* 2010; **16**(12)**:** 1393-1395.

37. Li H, Su P, Lai TK, Jiang A, Liu J, Zhai D *et al.* The glucocorticoid receptor-FKBP51 complex contributes to fear conditioning and posttraumatic stress disorder. *The Journal of clinical investigation* 2020; **130**(2)**:** 877-889.

38. Wang Y, Yan S, Zhang F, Li J, Li R, Zhang CX. Parkin-dependent and -independent degradation of synaptotagmin-11 in neurons and astrocytes. *Neuroscience letters* 2020; **739:** 135402.

39. Lee FH, Fadel MP, Preston-Maher K, Cordes SP, Clapcote SJ, Price DJ *et al.* Disc1 point mutations in mice affect development of the cerebral cortex. *The Journal of neuroscience : the official journal of the Society for Neuroscience* 2011; **31**(9)**:** 3197-3206.

40. Yang G, Pan F, Parkhurst CN, Grutzendler J, Gan WB. Thinned-skull cranial window technique for long-term imaging of the cortex in live mice. *Nature protocols* 2010; **5**(2)**:** 201-208.

41. Ma L, Qiao Q, Tsai JW, Yang G, Li W, Gan WB. Experience-dependent plasticity of dendritic spines of layer 2/3 pyramidal neurons in the mouse cortex. *Developmental neurobiology* 2016; **76**(3)**:** 277-286.

42. Li Y, Stockton ME, Bhuiyan I, Eisinger BE, Gao Y, Miller JL *et al.* MDM2 inhibition rescues neurogenic and cognitive deficits in a mouse model of fragile X syndrome. *Science translational medicine* 2016; **8**(336)**:** 336ra361.

43. Puighermanal E, Marsicano G, Busquets-Garcia A, Lutz B, Maldonado R, Ozaita A. Cannabinoid modulation of hippocampal long-term memory is mediated by mTOR signaling. *Nature neuroscience* 2009; **12**(9)**:** 1152-1158.

44. Contestabile A, Greco B, Ghezzi D, Tucci V, Benfenati F, Gasparini L. Lithium rescues synaptic plasticity and memory in Down syndrome mice. *The Journal of clinical investigation* 2013; **123**(1)**:** 348-361.

45. Hong S, Beja-Glasser VF, Nfonoyim BM, Frouin A, Li S, Ramakrishnan S *et al.* Complement and microglia mediate early synapse loss in Alzheimer mouse models. *Science* 2016; **352**(6286)**:** 712-716.

46. Stevens B, Allen NJ, Vazquez LE, Howell GR, Christopherson KS, Nouri N *et al.* The classical complement cascade mediates CNS synapse elimination. *Cell* 2007; **131**(6)**:** 1164-1178.

47. Bagni C, Greenough WT. From mRNP trafficking to spine dysmorphogenesis: the roots of fragile X syndrome. *Nature reviews Neuroscience* 2005; **6**(5)**:** 376-387.

48. Irwin SA, Patel B, Idupulapati M, Harris JB, Crisostomo RA, Larsen BP *et al.* Abnormal dendritic spine characteristics in the temporal and visual cortices of patients with fragile-X syndrome: a quantitative examination. *American journal of medical genetics* 2001; **98**(2)**:** 161-167.

49. Comery TA, Harris JB, Willems PJ, Oostra BA, Irwin SA, Weiler IJ *et al.* Abnormal dendritic spines in fragile X knockout mice: maturation and pruning deficits. *Proc Natl Acad Sci U S A* 1997; **94**(10)**:** 5401-5404.

50. McKinney BC, Grossman AW, Elisseou NM, Greenough WT. Dendritic spine abnormalities in the occipital cortex of C57BL/6 Fmr1 knockout mice. *American journal of medical genetics Part B, Neuropsychiatric genetics : the official publication of the International Society of Psychiatric Genetics* 2005; **136b**(1)**:** 98-102.

51. Pan F, Aldridge GM, Greenough WT, Gan WB. Dendritic spine instability and insensitivity to modulation by sensory experience in a mouse model of fragile X syndrome. *Proc Natl Acad Sci U S A* 2010; **107**(41)**:** 17768-17773.

52. Cruz-Martin A, Crespo M, Portera-Cailliau C. Delayed stabilization of dendritic spines in fragile X mice. *The Journal of neuroscience : the official journal of the Society for Neuroscience* 2010; **30**(23)**:** 7793-7803.

53. Padmashri R, Reiner BC, Suresh A, Spartz E, Dunaevsky A. Altered structural and functional synaptic plasticity with motor skill learning in a mouse model of fragile X syndrome. *The Journal of neuroscience : the official journal of the Society for Neuroscience* 2013; **33**(50)**:** 19715-19723.

54. Suresh A, Dunaevsky A. Relationship Between Synaptic AMPAR and Spine Dynamics: Impairments in the FXS Mouse. *Cerebral Cortex* 2017; **27**(8)**:** 4244-4256.

55. Wang H, Wu LJ, Kim SS, Lee FJ, Gong B, Toyoda H *et al.* FMRP acts as a key messenger for dopamine modulation in the forebrain. *Neuron* 2008; **59**(4)**:** 634-647.

56. Ito D, Imai Y, Ohsawa K, Nakajima K, Fukuuchi Y, Kohsaka S. Microglia-specific localisation of a novel calcium binding protein, Iba1. *Brain research Molecular brain research* 1998; **57**(1)**:** 1-9.

57. Xu R, Li X, Boreland AJ, Posyton A, Kwan K, Hart RP *et al.* Human iPSC-derived mature microglia retain their identity and functionally integrate in the chimeric mouse brain. *Nat Commun* 2020; **11**(1)**:** 1577.

58. Hopperton KE, Mohammad D, Trépanier MO, Giuliano V, Bazinet RP. Markers of microglia in post-mortem brain samples from patients with Alzheimer's disease: a systematic review. *Mol Psychiatry* 2018; **23**(2)**:** 177-198.

59. Paolicelli RC, Bolasco G, Pagani F, Maggi L, Scianni M, Panzanelli P *et al.* Synaptic pruning by microglia is necessary for normal brain development. *Science* 2011; **333**(6048)**:** 1456-1458.

60. Schafer DP, Lehrman EK, Kautzman AG, Koyama R, Mardinly AR, Yamasaki R *et al.* Microglia sculpt postnatal neural circuits in an activity and complement-dependent manner. *Neuron* 2012; **74**(4)**:** 691-705.

61. Stephan AH, Barres BA, Stevens B. The complement system: an unexpected role in synaptic pruning during development and disease. *Annual review of neuroscience* 2012; **35:** 369-389.

62. Chu Y, Jin X, Parada I, Pesic A, Stevens B, Barres B *et al.* Enhanced synaptic connectivity and epilepsy in C1q knockout mice. *Proc Natl Acad Sci U S A* 2010; **107**(17)**:** 7975-7980.

63. Bialas AR, Stevens B. TGF-β signaling regulates neuronal C1q expression and developmental synaptic refinement. *Nature neuroscience* 2013; **16**(12)**:** 1773-1782.

64. Datta D, Leslie SN, Morozov YM, Duque A, Rakic P, van Dyck CH *et al.* Classical complement cascade initiating C1q protein within neurons in the aged rhesus macaque dorsolateral prefrontal cortex. *Journal of neuroinflammation* 2020; **17**(1)**:** 8.

65. Dejanovic B, Huntley MA, De Mazière A, Meilandt WJ, Wu T, Srinivasan K *et al.* Changes in the Synaptic Proteome in Tauopathy and Rescue of Tau-Induced Synapse Loss by C1q Antibodies. *Neuron* 2018; **100**(6)**:** 1322-1336.e1327.

66. Schreiber J, Vegh MJ, Dawitz J, Kroon T, Loos M, Labonte D *et al.* Ubiquitin ligase TRIM3 controls hippocampal plasticity and learning by regulating synaptic gamma-actin levels. *The Journal of cell biology* 2015; **211**(3)**:** 569-586.

67. Penzes P, Cahill ME, Jones KA, VanLeeuwen JE, Woolfrey KM. Dendritic spine pathology in neuropsychiatric disorders. *Nature neuroscience* 2011; **14**(3)**:** 285-293.

68. Pfeiffer BE, Zang T, Wilkerson JR, Taniguchi M, Maksimova MA, Smith LN *et al.* Fragile X mental retardation protein is required for synapse elimination by the activity-dependent transcription factor MEF2. *Neuron* 2010; **66**(2)**:** 191-197.

69. Benger M, Kinali M, Mazarakis ND. Autism spectrum disorder: prospects for treatment using gene therapy. *Mol Autism* 2018; **9:** 39.

70. Pena SA, Iyengar R, Eshraghi RS, Bencie N, Mittal J, Aljohani A *et al.* Gene therapy for neurological disorders: challenges and recent advancements. *J Drug Target* 2020; **28**(2)**:** 111-128.

71. Mendell JR, Al-Zaidy S, Shell R, Arnold WD, Rodino-Klapac LR, Prior TW *et al.* Single-Dose Gene-Replacement Therapy for Spinal Muscular Atrophy. *N Engl J Med* 2017; **377**(18)**:** 1713-1722.

72. Barash Y, Calarco JA, Gao W, Pan Q, Wang X, Shai O *et al.* Deciphering the splicing code. *Nature* 2010; **465**(7294)**:** 53-59.

73. Zhai D, Lee FHF, D'Souza C, Su P, Zhang S, Jia Z *et al.* Blocking GluR2–GAPDH ameliorates experimental autoimmune encephalomyelitis. *Annals of Clinical and Translational Neurology* 2015; **2**(4)**:** 388-400.

Figure Legends

Figure 1. Molecular characterization of Mdm2-EF1α and TRIM3- EF1α complexes.

A. In mouse brain lysate, Mdm2 antibody, but not IgG (negative control), co-immunoprecipitated with EF1α (top), while EF1α antibody co-immunoprecipitated with Mdm2 (bottom). Blots represent 3 independent experiments performed.

B. Co-immunoprecipitation showed that the level of Mdm2-EF1α complex increased in *Fmr1* KO mice as compared to levels in wild-type (WT) mice.

C. Densitometric analysis of Mdm2 co-immunoprecipitated by EF1α from brain lysates of WT or *Fmr1* KO mice. The level of co-immunoprecipitated Mdm2 (Mdm2 CO-IP) was normalized to

the level of immunoprecipitated EF1α (EF1α IP). Results for each sample are presented as the percentage of the wild-type (WT) sample. Data were analyzed by t-test, $*p < 0.05$, $n = 3$ mice per group. Data are shown as mean ± S.E.M.

D. In mouse brain lysate, TRIM3 antibody, but not IgG (negative control), co-immunoprecipitated with EF1α (top); while EF1α antibody co-immunoprecipitated with TRIM3 (bottom). Blots represent 3 independent experiments performed.

E. Co-immunoprecipitation showed that the level of TRIM3-EF1α complex is increased in *Fmr1* KO mice as compared to wild-type (WT) mice.

F. Densitometric analysis of EF1α co-immunoprecipitated by TRIM3 from brain lysates of WT or *Fmr1* KO mice. The level of co-immunoprecipitated EF1α (EF1α CO-IP) was normalized to the level of immunoprecipitated TRIM3 (TRIM3 IP). Results for each sample are presented as the percentage of the wild-type (WT) sample. Data were analyzed by t-test, $*p < 0.05$, $n = 3$ mice per group. Data are shown as mean ± S.E.M.

G. Representative images of TRIM3-EF1α (top) and Mdm2-EF1α (middle) complexes in the same amount of protein extracted from the same samples of WT and *Fmr1* KO mouse brain tissue. The total expression levels of EF1α (bottom) in each sample are also shown.

H. Densitometric analysis of the ratio of EF1α-TRIM3 complex *vs.* total expression level of EF1α in brain lysates of WT and *Fmr1* KO mice. The level of EF1α co-immunoprecipitated by TRIM3 (EF1α-Trim3 complex) was divided by the total amount of EF1α (Total EF1α). Results for each sample are presented as the percentage of the wild-type (WT) samples. Data were analyzed by t-test, $**p < 0.01$, $n = 3$ mice per group. Data are shown as mean ± S.E.M.

I. Densitometric analysis of the ratio of EF1α-Mdm2 complex *vs* total expression level of EF1α in brain lysate of WT and *Fmr1* KO mice. The level of EF1α co-immunoprecipitated by Mdm2

(EF1α-Mdm2 complex) was divided by the total level of EF1α (Total EF1α). Results for each sample are presented as the percentage of the wild-type (WT) samples. Data were analyzed by t-test, $*p < 0.05$, $n = 3$ mice in each group. Data are shown as mean ± S.E.M.

Figure 2. Both Mdm2 and TRIM3 form protein complexes with EF1α via the L77-D91 region of EF1α.

A. Western blot showing that GST-EF1α-1, but not GST, GST-EF1α-2, GST-EF1α-3, or GST-EF1α-4, was able to "pull down" Mdm2 from mouse brain lysate. Blots represent 3 independent experiments performed.

B. Western blot showing that GST-EF1α-1-2, but not GST, GST-EF1α-1-1, GST-EF1α-1-3, or GST-EF1α-1-4, was able to "pull down" Mdm2 from mouse brain lysate. Blots represent 3 independent experiments performed.

C. Western blot showing that GST-EF1α-1-2-2, but not GST, GST-EF1α-1-2-1, GST-EF1α-1-2-3, or GST-EF1α-1-2-4, was able to "pull down" Mdm2 from mouse brain lysate. Blots represent 3 independent experiments performed.

D. Western blot analysis of Mdm2 co-immunoprecipitated by EF1α-specific antibody from wild-type mouse brain lysate in the presence or absence of TAT-EF1α. Blots represent 3 independent experiments performed.

E. Western blot showing that GST-EF1α-1, but not GST, GST-EF1α-2, GST-EF1α-3, or GST-EF1α-4, was able to "pull down" TRIM3 from mouse brain lysate. Blots represent 3 independent experiments performed.

F. Western blot showing that GST-EF1α-1-2, but not GST, GST-EF1α-1-1, GST-EF1α-1-3, or GST-EF1α-1-4, was able to "pull down" TRIM3 from mouse brain lysate. Blots represent 3 independent experiments performed.

G. Western blot showing that GST-EF1α-1-2-2, but not GST, GST-EF1α-1-2-1, GST-EF1α-1-2-3, or GST-EF1α-1-2-4, was able to "pull down" TRIM3 from mouse brain lysate. Blots represent 3 independent experiments performed.

H. Western blot analysis of EF1α co-immunoprecipitated by TRIM3-specific antibody from wild-type mouse brain lysate in the presence or absence of TAT-EF1α. Blots represent 3 independent experiments performed.

I. Co-immunoprecipitation showed that TAT-EF1α is able to disrupt the Mdm2-EF1α complex in *Fmr1* KO mice as compared to control treatment with saline or TAT.

J. Densitometric analysis of Mdm2 co-immunoprecipitated by EF1α from brain lysate of *Fmr1* KO mice injected with saline, TAT, or TAT-EF1α peptide. The level of co-immunoprecipitated Mdm2 (Mdm2 Co-IP) was normalized after being divided by the level of directly immunoprecipitated EF1α (EF1α IP). Results for each sample are presented as the percentage of the wild-type (WT) samples. Data were analyzed by one-way *ANOVA*, $***p < 0.001$ as compared to WT group, $\#p < 0.05$ as compared to KO + Saline group, $n = 3$ mice in each group. Data are shown as mean ± S.E.M.

K. Co-immunoprecipitation showed that TAT-EF1α disrupts the TRIM3-EF1α complex in *Fmr1* KO mice as compared to control treatment with saline or TAT.

L. Densitometric analysis of EF1α co-immunoprecipitated by TRIM3 from brain lysate of *Fmr1* KO mice injected with saline, TAT, or TAT-EF1α peptide. The level of co-immunoprecipitated EF1α (EF1α Co-IP) was normalized after being divided by the level of immunoprecipitated TRIM3 (TRIM3 IP). Results for each sample are presented as the percentage of the WT samples in Figure 1E-F. Data were analyzed by one-way *ANOVA*, $***p < 0.001$ as compared to KO + Saline group, $n = 4$ mice per group. Data are shown as mean ± S.E.M.

Figure 3. TAT-EF1α peptide restores dendritic spine density and plasticity, and reverses behavioural deficits in *Fmr1* KO mice.

A. Representative images of dendritic spines in the frontal cortex visualized with Golgi-Cox staining. Scale bar: 2 μm. 100 × magnification.

B. Quantification of dendritic spine density, measured as the number of spines per 10 μm of dendrite length. Results for each sample are presented as the percentage of the wild-type (WT) samples. Data were analyzed by one-way ANOVA, ***$p < 0.001$ as compared to WT group, ### $p < 0.001$ as compared to KO + Saline group. n = 26–35 images from 3 mice per group. Data are shown as mean ± S.E.M.

C. Schematic showing the timeline of peptide administration and *in vivo* longitudinal imaging of synaptic structural plasticity in *Thy1*-YFP transgenic mice, which express yellow fluorescent protein (YFP) in L5 pyramidal neurons. *Fmr1* KO mice received daily intraperitoneal (*i.p.*) injections of saline, TAT-EF1α or TAT from P14 to P20.

D. Representative images of transcranial two-photon imaging of dendritic spines on apical dendritic segments of L5 pyramidal neurons in the frontal association cortex of WT and *Fmr1* KO mice with various treatments. Empty and filled arrowheads indicate individual spines that were eliminated or newly formed, respectively, on the same dendritic segment over 2 days. Asterisks indicate dendritic filopodia. Scale bar, 2 μm.

E. Summary quantification of dendritic spine elimination and formation from P21 to P23 in WT and *Fmr1* KO mice with various treatments. n = 5–6 mice per group.

F. Spine elimination and formation from P21 to P31 in WT and *Fmr1* KO mice with various treatments. n = 5–6 mice per group.

G. Apical dendritic spine density in the frontal cortex on P31. n = 5–6 mice per group.

Data are presented as mean ± S.E.M. *P < 0.05, **P < 0.01, ***P < 0.001, by one-way ANOVA followed by Bonferroni's multiple comparisons test.

H. TAT-EF1α injection increased the time *Fmr1* KO mice spent in open maze arms per entry in the elevated plus-maze as compared to control treatment with either TAT or saline. Data were analyzed by one-way *ANOVA*, *p < 0.05, ****p < 0.0001 as compared to WT group, ### p < 0.001 as compared to KO + Saline group. n = 8 mice per group. Data are shown as mean ± S.E.M.

I. TAT-EF1α peptide treatment rescued deficits in the novel object recognition test in *Fmr1* KO mice as compared to those injected with either TAT or saline. Data were analyzed by one-way *ANOVA*, *p < 0.05, **p < 0.01 as compared to WT group, # p < 0.05 as compared to KO + Saline group. n = 8 mice per group. Data are shown as mean ± S.E.M.

J. TAT-EF1α peptide treatment rescued spatial learning deficits in *Fmr1* KO mice in the displaced object test, as compared to those injected with either TAT or saline. Data were analyzed by one-way *ANOVA*, *p < 0.05, ****p < 0.0001 as compared to WT group, ### p < 0.001 as compared to KO + Saline group. n = 8 mice per group. Data are shown as mean ± S.E.M.

K. Preference for social novelty was assessed in the three-chamber social interaction test by measuring the time the test mouse spent with the second stranger mouse (stranger 2, S2) or the previously encountered mouse (Stranger 1, S1). TAT-EF1α peptide treatment rescued deficits in social behaviour as compared to those injected with either TAT or saline. Data were analyzed by two-way *ANOVA*, **p < 0.01, ***p < 0.001 as compared to WT group, n = 8 mice per group. Data are shown as mean ± S.E.M.

Figure 4. TAT-EF1α-pep rescued microglial synaptic pruning deficiency in cortex of *Fmr1* KO mice at postnatal day 21 and normalizes the amount of Mdm2-PSD95 complex, ubiquitination of PSD95 and PSD95-C1q interaction in *Fmr1* KO mice.

A. Representative confocal images of staining with antibody against Iba1 (red) and PSD95 (green) in P21 WT, Fmr1-KO, KO+TAT, KO+TAT-EF1α treated mice. Images show higher magnification of the inset images in the right corner. Scale bar: 20 μm.

B. Quantification shows the fraction of Iba1 overlapping PSD95. N = 26 / 22 / 23 / 29 views from 3 mice per group, ****p < 0.0001 compared to WT, #### p < 0.0001 compared to KO + Saline, $$p = 0.0014 compared to KO + TAT, $F_{3,96} = 3.997$, one-way ANOVA.

C. Representative 3D reconstruction of super-resolution images showing PSD95 (green) engulfed within microglia in P21 WT, KO + Saline, KO + TAT, KO + TAT-EF1α treated mice. Scale bar: 5 μm.

D. Quantification of the percentage of total microglial volume occupied by PSD95 . n =13 / 11 / 11 / 15 views from 2-3 mice per group, *p = 0.015 compare to WT, **p = 0.0051 compared to WT, #p = 0.0192 compared to KO + Saline, $$p = 0.0064 compared to KO + TAT, $F_{3,46} = 1.590$, one-way ANOVA.

E. Co-immunoprecipitation showing that TAT-EF1α increases the Mdm2-PSD95 interaction in *Fmr1* KO mice as compared to levels in saline or TAT-injected control groups.

F. Densitometric analysis of Mdm2 co-immunoprecipitated by PSD95 from brain lysates of *Fmr1* KO mice injected with saline, TAT, or TAT-EF1α peptide. The level of co-immunoprecipitated Mdm2 (Mdm2 Co-IP) was normalized to the level of immunoprecipitated PSD95 (PSD95 IP). Results for each sample are presented as the percentage of the WT samples. Data were analyzed by one-way *ANOVA*, *$p < 0.05$, **p < 0.01 as compared to WT

group, ###p < 0.001 as compared to KO + Saline group, *n* = 3 mice per group. Data are shown as mean ± S.E.M.

G. Immunoprecipitation showed that TAT-EF1α increases the ubiquitination of PSD95 in *Fmr1* KO mice as compared to control treatment with saline or TAT.

H. Densitometric analysis of the levels of ubiquitinated PSD95 in brain lysates of *Fmr1* KO mice injected with saline, TAT, or TAT-EF1α peptide. Results for each sample are presented as the percentage of the WT samples. Data were analyzed by one-way *ANOVA*, *$p < 0.05$, **p < 0.01 as compared to WT group, ###p < 0.001 as compared to KO + Saline group, *n* = 3 mice per group. Data are shown as mean ± S.E.M.

I. Representative high-resolution confocal imaging shows colocalization of PSD95 (red) and C1q (green) in the cortex of P21 *Fmr1* KO mice injected with either saline, TAT, or TAT-EF1α peptide, as well as in WT mice. Scale bar: 4 μm.

J. Quantification of overlapping puncta between C1q and the synaptic markers PSD-95 (n = 4 mice per group, four sections per mouse. Scale bar = 4 μm; *p < 0.05, ***p < 0.001 compared to WT, $F_{3,96}$=6.82, one-way ANOVA). Data are shown as mean ± S.E.M.

K. Co-immunoprecipitation showed that Nutlin-3 treatment (5 μM, 1 hour) decreases the PSD95-C1q interaction in mouse brain slices.

L. Densitometric analysis of C1q co-immunoprecipitated by PSD95 from lysate of mouse brain slices treated with vehicle (control) or Nutlin-3. Results for each sample are presented as the percentage of the control samples. Data were analyzed by t-test, **p < 0.01 as compared to control group, *n* = 4 mice per group. Data are shown as mean ± S.E.M.

Figure 5. TAT-EF1α peptide facilitates C3 cleavage through regulating the TRIM3-C3 complex in *Fmr1* KO mice.

A. Co-immunoprecipitation shows decreased levels of TRIM3-C3 complex in *Fmr1* KO mice.

B. Densitometric analysis of C3 co-immunoprecipitated by TRIM3 from brain lysates of WT or *Fmr1* KO mice. The level of co-immunoprecipitated C3 (C3 CO-IP) was normalized to the level of immunoprecipitated TRIM3 (Trim3 IP). Results for each sample are presented as the percentage of the wild-type (WT) samples. Data were analyzed by t-test, $*p < 0.05$, $n = 3$ mice per group. Data are shown as mean ± S.E.M.

C. Co-immunoprecipitation showed that TAT-EF1α increases the levels of TRIM3-C3 complex in *Fmr1* KO mice as compared to control treatment with saline or TAT.

D. Densitometric analysis of C3 co-immunoprecipitated by TRIM3 from brain lysates of *Fmr1* KO mice injected with saline, TAT, or TAT-EF1α peptide. The level of co-immunoprecipitated C3 (C3 Co-IP) was normalized to the level of immunoprecipitated TRIM3 (TRIM3 IP). Results for each sample are presented as the percentage of the WT samples in Figure 5A-B. Data were analyzed by one-way *ANOVA*, $***p < 0.001$ as compared to KO + Saline group, $n = 4$ mice per group. Data are shown as mean ± S.E.M.

E. Western blot analysis showed that TAT-EF1α decreases the levels of full-length C3, but increases the levels of C3 cleavage in *Fmr1* KO mice, as compared to control treatment with saline or TAT. α-Tubulin was used as a loading control.

F. Densitometric analysis of the levels of full-length C3 in brain lysates of *Fmr1* KO mice injected with saline, TAT, or TAT-EF1α peptide, as well as WT mice. The level of full-length C3 was normalized to the level of α-Tubulin. Results for each sample are presented as the percentage of the WT samples. Data were analyzed by one-way *ANOVA*, $*p < 0.05$ as compared to WT group, $\#p < 0.05$ as compared to KO + Saline group, $n = 3$ mice per group. Data are shown as mean ± S.E.M.

G. Densitometric analysis of the levels of C3 cleaved fragment in brain lysates of *Fmr1* KO mice injected with saline, TAT, or TAT-EF1α peptide, as well as WT mice. The level of C3 cleaved fragment was normalized after being divided by the level of α-Tubulin. Results for each sample are presented as the percentage of the WT samples. Data were analyzed by one-way *ANOVA*, $*p < 0.05$ as compared to WT group, ###p < 0.001 as compared to KO + Saline group, $n = 3$ mice per group. Data are shown as mean ± S.E.M.

H. Western blot analysis showing that knockdown of TRIM3 expression with Trim3 siRNA decreases C3 cleavage in primarily cultured cortical neurons. α-Tubulin was used as a loading control.

I. Densitometric analysis of the levels of iC3b in primary cortical neuron cultures treated with control siRNA or Trim3 siRNA. The level of iC3b was normalized to the level of α-Tubulin. Results for each sample are presented as the percentage of the control siRNA (CTRL siRNA) samples. Data were analyzed by t-test, $**p < 0.01$ as compared to CTRL siRNA group, $n = 3$ biological repeats per group. Data are shown as mean ± S.E.M.

J. Densitometric analysis of the levels of C3 cleaved fragment in primary cortical neuron cultures treated with control siRNA or Trim3 siRNA. The level of C3 cleaved fragment was normalized to the level of α-Tubulin. Results for each sample are presented as the percentage of the control siRNA (CTRL siRNA) samples. Data were analyzed by t-test, $*p < 0.05$ as compared to CTRL siRNA group, $n = 3$ biological repeats per group. Data are shown as mean ± S.E.M.

K. Densitometric analysis of the expression levels of TRIM3 in primary cortical neuron cultures treated with control siRNA or Trim3 siRNA. The level of Trim3 was normalized to the level of α-Tubulin. Results for each sample are presented as the percentage of the control siRNA

(CTRL siRNA) samples. Data were analyzed by t-test, $*p < 0.05$ as compared to CTRL siRNA group, $n = 3$ biological repeats per group. Data are shown as mean ± S.E.M.

Figure 6. Schematic model showing the hypothesized pathway by which Mdm2-EF1α and TRIM3-EF1α regulate dendritic spine density and plasticity.

Conditions favouring synapse elimination in control mice are shown in the top panel. Briefly, Mdm2 functions as a ubiquitin E3 ligase, binding with ubiquitinated (Ub) PSD-95 in the dendritic spine, which complexes further with Pchd10 and the proteosome to degrade that spine. At the same time, Ub-PSD-95 binds C1q, the initial component of the complement cascade that signals through C3 and the CR3 receptor on microglia to trigger phagocytosis. TRIM3 also binds to C3 and contributes to activation of the complement cascade, acting synergistically with the Ub-PSD-95-C1q complex to drive phagocytosis and degradation of the dendritic spine. Conversely, the conditions that inhibit synaptic pruning in *Fmr1* KO mice and stabilize dendritic spines are shown in the bottom panel. Loss of FMRP removes translational suppression of eukaryotic translation elongation factor 1-α (*EF1α*). The increased amounts of EF1α bind to and sequester both Mdm2 and TRIM3, preventing them from binding with PSD-95 or C3, thus inhibiting spine degradation and phagocytosis by microglia.

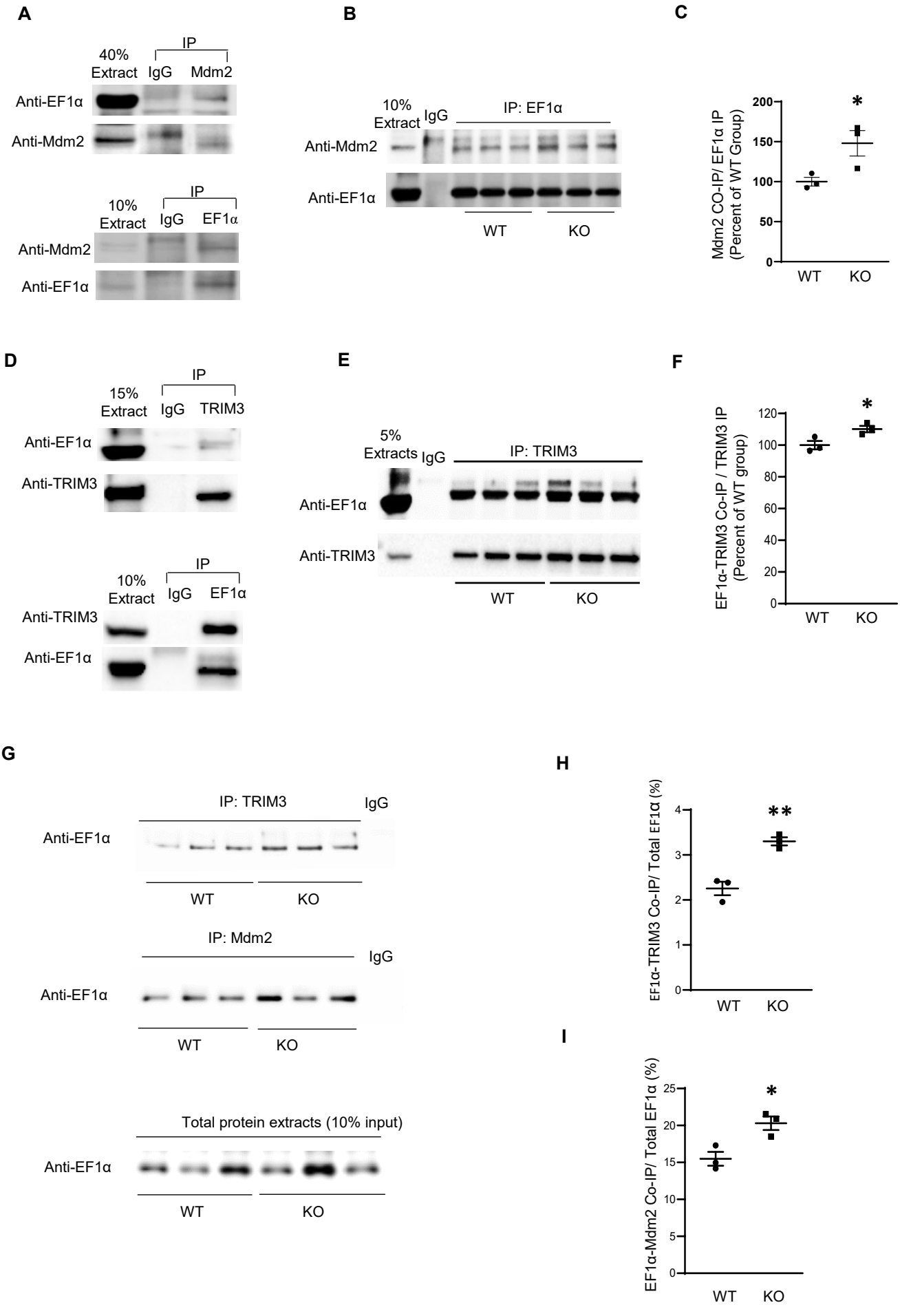
A
40% Extract
IP
IgG
Mdm2
Anti-EF1α
Anti-Mdm2
10% Extract
IP
IgG
EF1α
Anti-Mdm2
Anti-EF1α
B
10% Extract
IgG
IP: EF1α
Anti-Mdm2
Anti-EF1α
WT
KO
C
Mdm2 CO-IP/ EF1α IP (Percent of WT Group)
200
150
100
50
0
*
WT
KO
D
15% Extract
IP
IgG
TRIM3
Anti-EF1α
Anti-TRIM3
10% Extract
IP
IgG
EF1α
Anti-TRIM3
Anti-EF1α
E
5% Extracts
IgG
IP: TRIM3
Anti-EF1α
Anti-TRIM3
WT
KO
F
EF1α-TRIM3 Co-IP / TRIM3 IP (Percent of WT group)
120
100
80
60
40
20
0
*
WT
KO
G
IP: TRIM3
IgG
Anti-EF1α
WT
KO
IP: Mdm2
IgG
Anti-EF1α
WT
KO
Total protein extracts (10% input)
Anti-EF1α
WT
KO
H
EF1α-TRIM3 Co-IP/ Total EF1α (%)
4
3
2
1
0
**
WT
KO
I
EF1α-Mdm2 Co-IP/ Total EF1α (%)
25
20
15
10
5
0
*
WT
KO

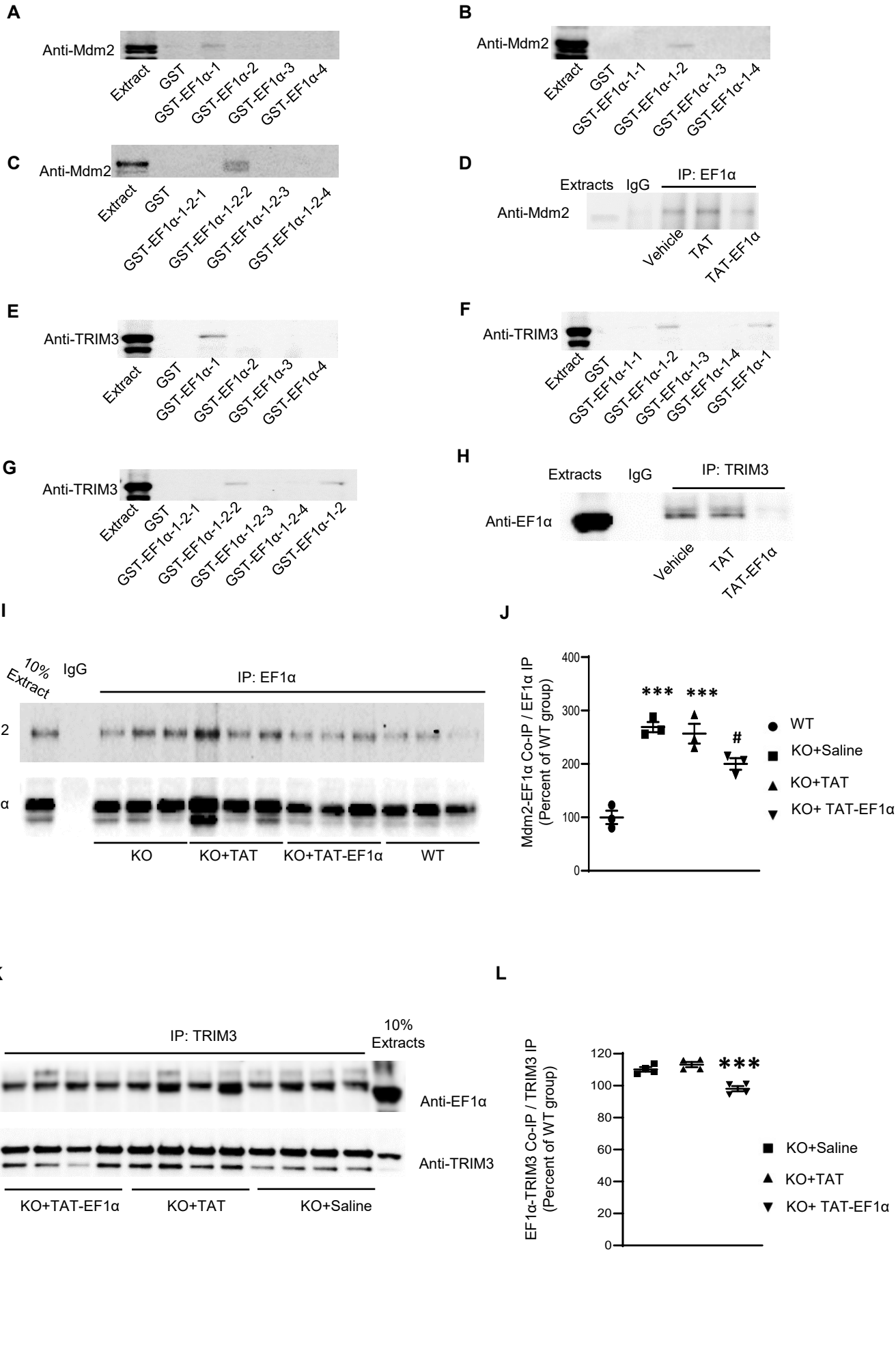
A
Anti-Mdm2
Extract
GST
GST-EF1α-1
GST-EF1α-2
GST-EF1α-3
GST-EF1α-4
B
Anti-Mdm2
Extract
GST
GST-EF1α-1-1
GST-EF1α-1-2
GST-EF1α-1-3
GST-EF1α-1-4
C
Anti-Mdm2
Extract
GST
GST-EF1α-1-2-1
GST-EF1α-1-2-2
GST-EF1α-1-2-3
GST-EF1α-1-2-4
D
Extracts
IgG
IP: EF1α
Anti-Mdm2
Vehicle
TAT
TAT-EF1α
E
Anti-TRIM3
Extract
GST
GST-EF1α-1
GST-EF1α-2
GST-EF1α-3
GST-EF1α-4
F
Anti-TRIM3
Extract
GST
GST-EF1α-1-1
GST-EF1α-1-2
GST-EF1α-1-3
GST-EF1α-1-4
GST-EF1α-1
G
Anti-TRIM3
Extract
GST
GST-EF1α-1-2-1
GST-EF1α-1-2-2
GST-EF1α-1-2-3
GST-EF1α-1-2-4
GST-EF1α-1-2
H
Extracts
IgG
IP: TRIM3
Anti-EF1α
Vehicle
TAT
TAT-EF1α
I
10% Extract
IgG
IP: EF1α
Anti-Mdm2
Anti-EF1α
KO
KO+TAT
KO+TAT-EF1α
WT
J
Mdm2-EF1α Co-IP / EF1α IP (Percent of WT group)
400
300
200
100
0
***
***
#
WT
KO+Saline
KO+TAT
KO+ TAT-EF1α
K
IgG
IP: TRIM3
10% Extracts
Anti-EF1α
Anti-TRIM3
KO+TAT-EF1α
KO+TAT
KO+Saline
L
EF1α-TRIM3 Co-IP / TRIM3 IP (Percent of WT group)
120
100
80
60
40
20
0
***
KO+Saline
KO+TAT
KO+ TAT-EF1α

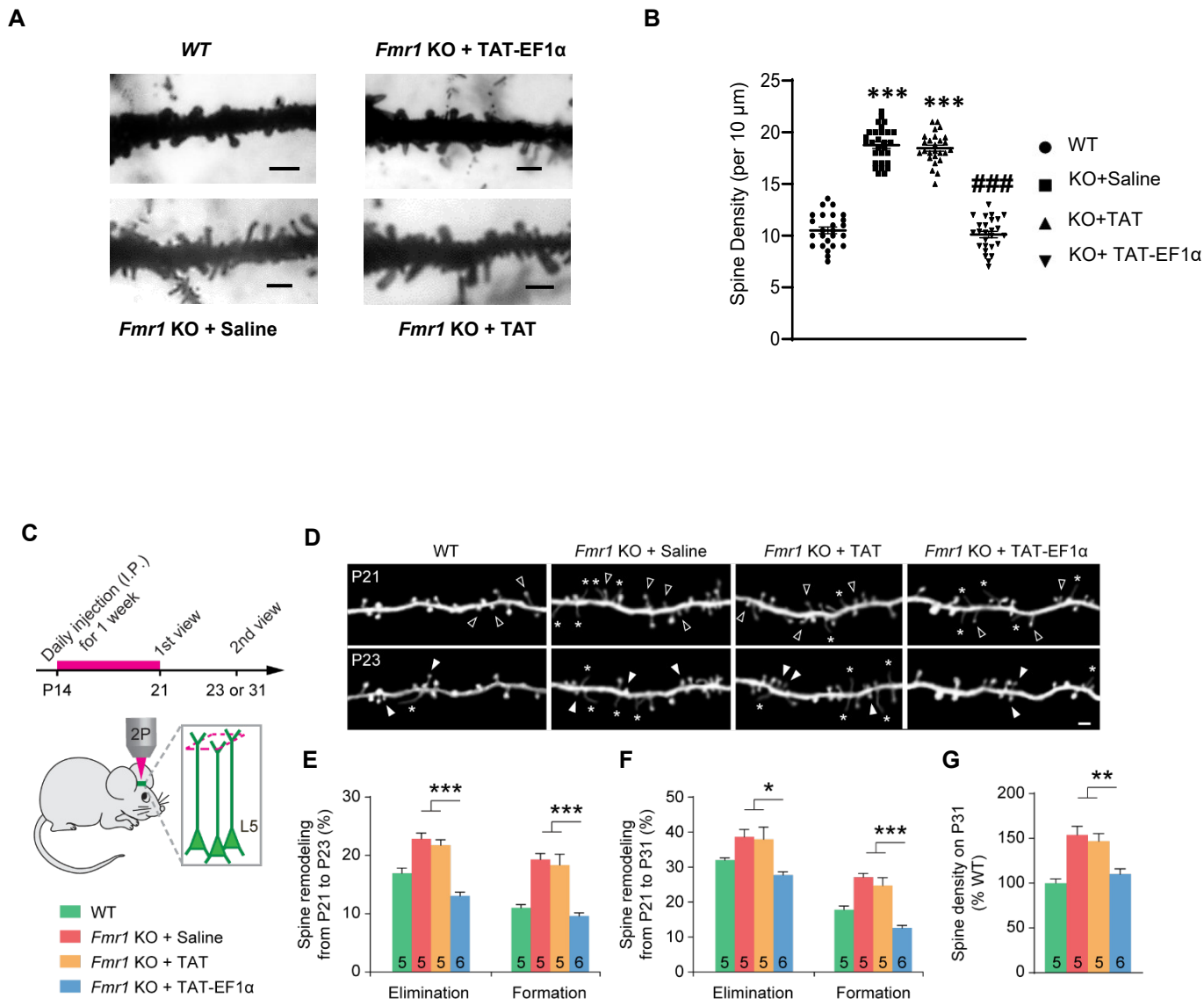
A
WT
Fmr1 KO + TAT-EF1α
Fmr1 KO + Saline
Fmr1 KO + TAT
B
Spine Density (per 10 μm)
25
20
15
10
5
0
***
***
###
WT
KO+Saline
KO+TAT
KO+ TAT-EF1α
C
Daily injection (I.P.) for 1 week
1st view
2nd view
P14
21
23 or 31
2P
L5
WT
Fmr1 KO + Saline
Fmr1 KO + TAT
Fmr1 KO + TAT-EF1α
D
WT
Fmr1 KO + Saline
Fmr1 KO + TAT
Fmr1 KO + TAT-EF1α
P21
P23
E
Spine remodeling from P21 to P23 (%)
30
20
10
0
***
***
5 5 5 6
5 5 5 6
Elimination
Formation
F
Spine remodeling from P21 to P31 (%)
50
40
30
20
10
0
*
***
5 5 5 6
5 5 5 6
Elimination
Formation
G
Spine density on P31 (% WT)
200
150
100
50
0
**
5 5 5 6

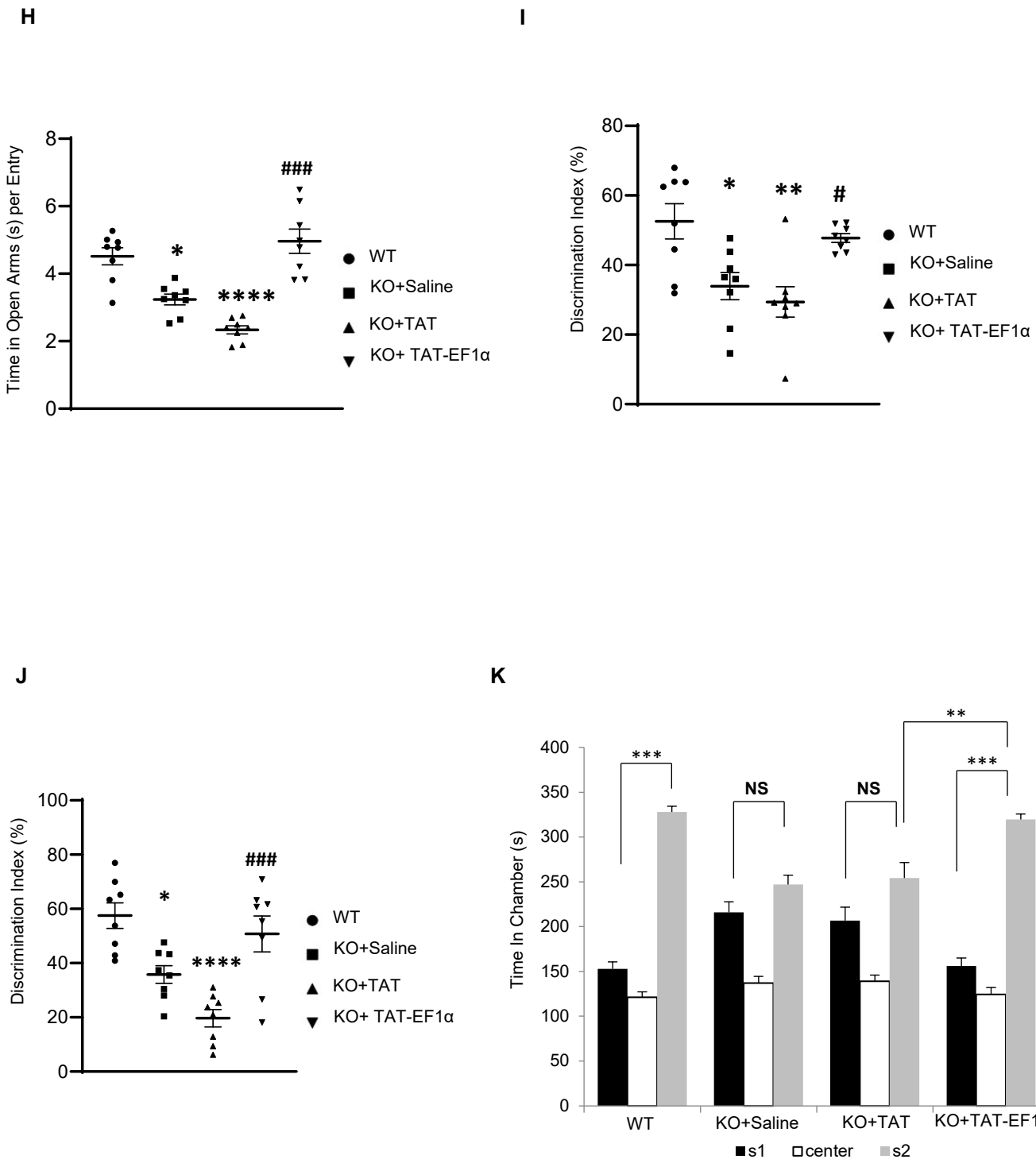
H
Time in Open Arms (s) per Entry
8
6
4
2
0
*
****
###
WT
KO+Saline
KO+TAT
KO+ TAT-EF1α
I
Discrimination Index (%)
80
60
40
20
0
*
**
#
WT
KO+Saline
KO+TAT
KO+ TAT-EF1α
J
Discrimination Index (%)
100
80
60
40
20
0
*
****
###
WT
KO+Saline
KO+TAT
KO+ TAT-EF1α
K
Time In Chamber (s)
400
350
300
250
200
150
100
50
0
***
NS
NS
**
***
WT
KO+Saline
KO+TAT
KO+TAT-EF1α
s1
center
s2

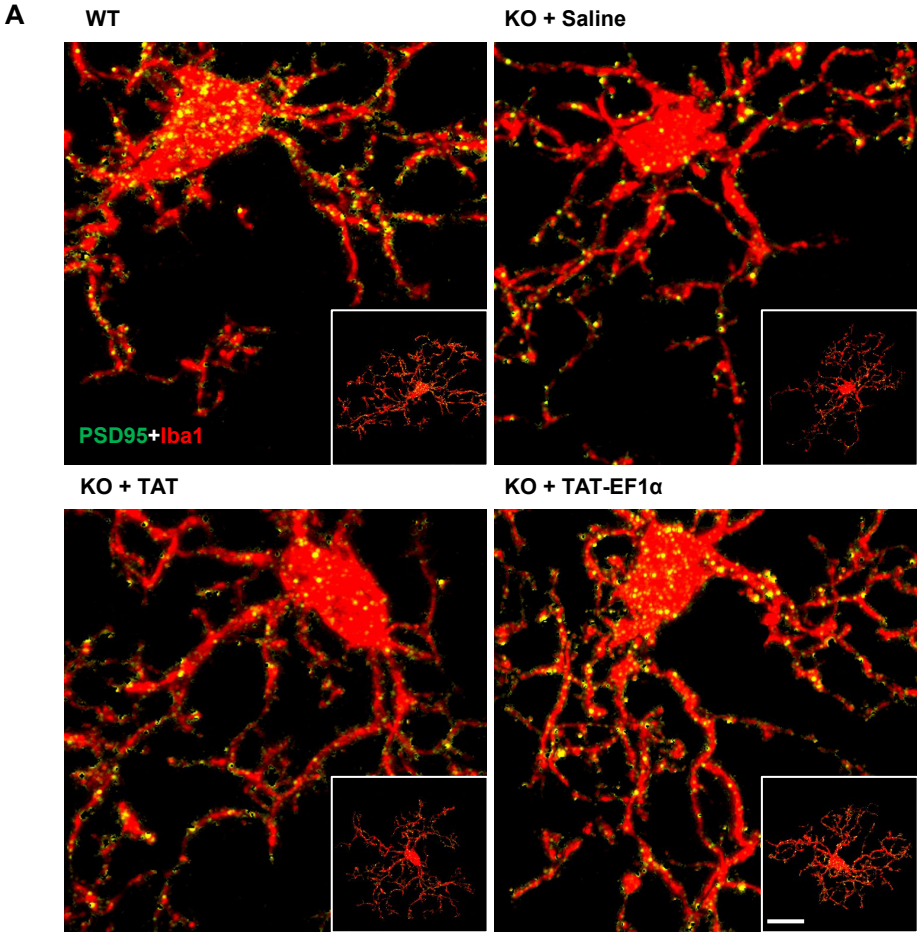
A
WT
KO + Saline
PSD95+Iba1
KO + TAT
KO + TAT-EF1α

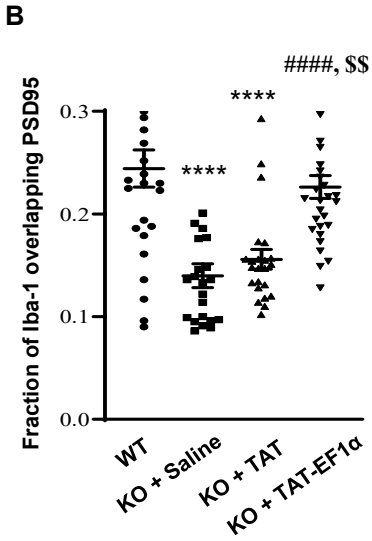
B
####, $$
****
****
Fraction of Iba-1 overlapping PSD95
0.3
0.2
0.1
0.0
WT
KO + Saline
KO + TAT
KO + TAT-EF1α

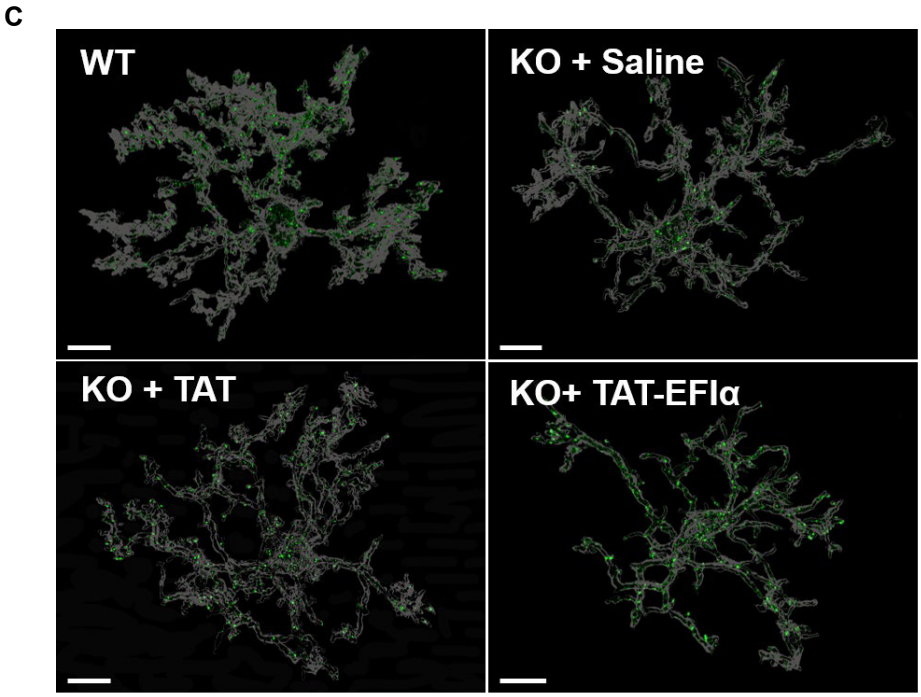
C
WT
KO + Saline
KO + TAT
KO+ TAT-EFIα

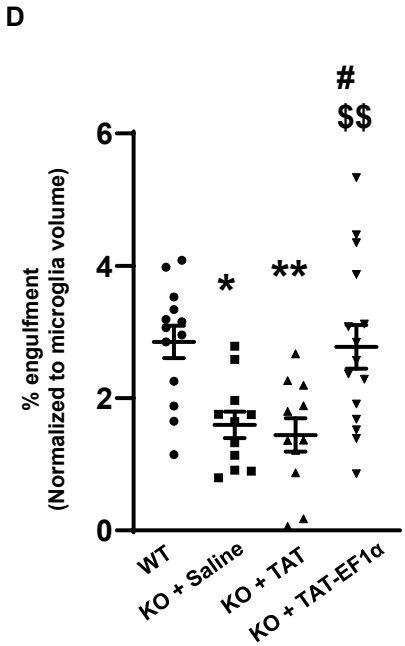
D
#
$$
*
**
% engulfment
(Normalized to microglia volume)
6
4
2
0
WT
KO + Saline
KO + TAT
KO + TAT-EF1α

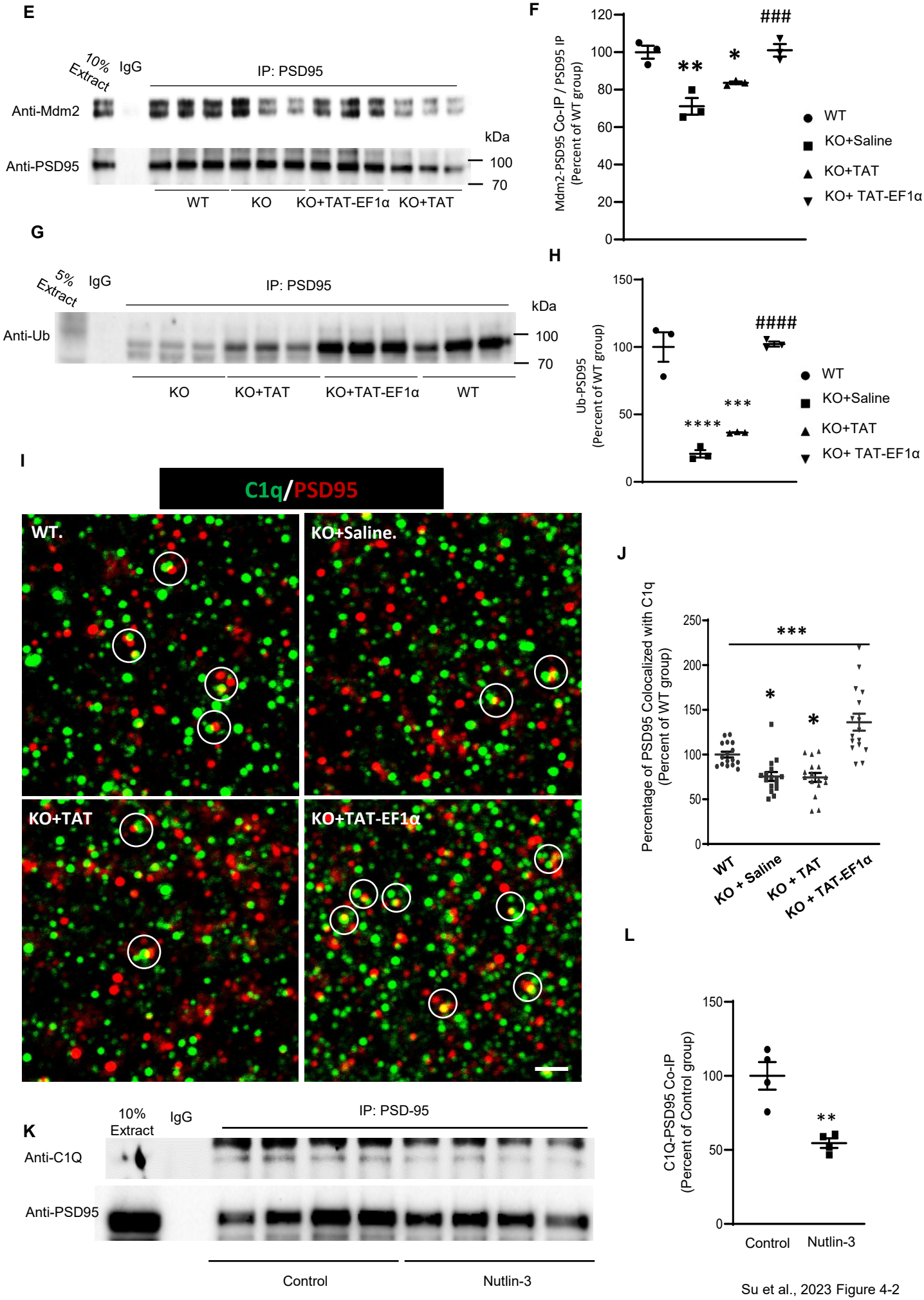

Su et al., 2023 Figure 4-2

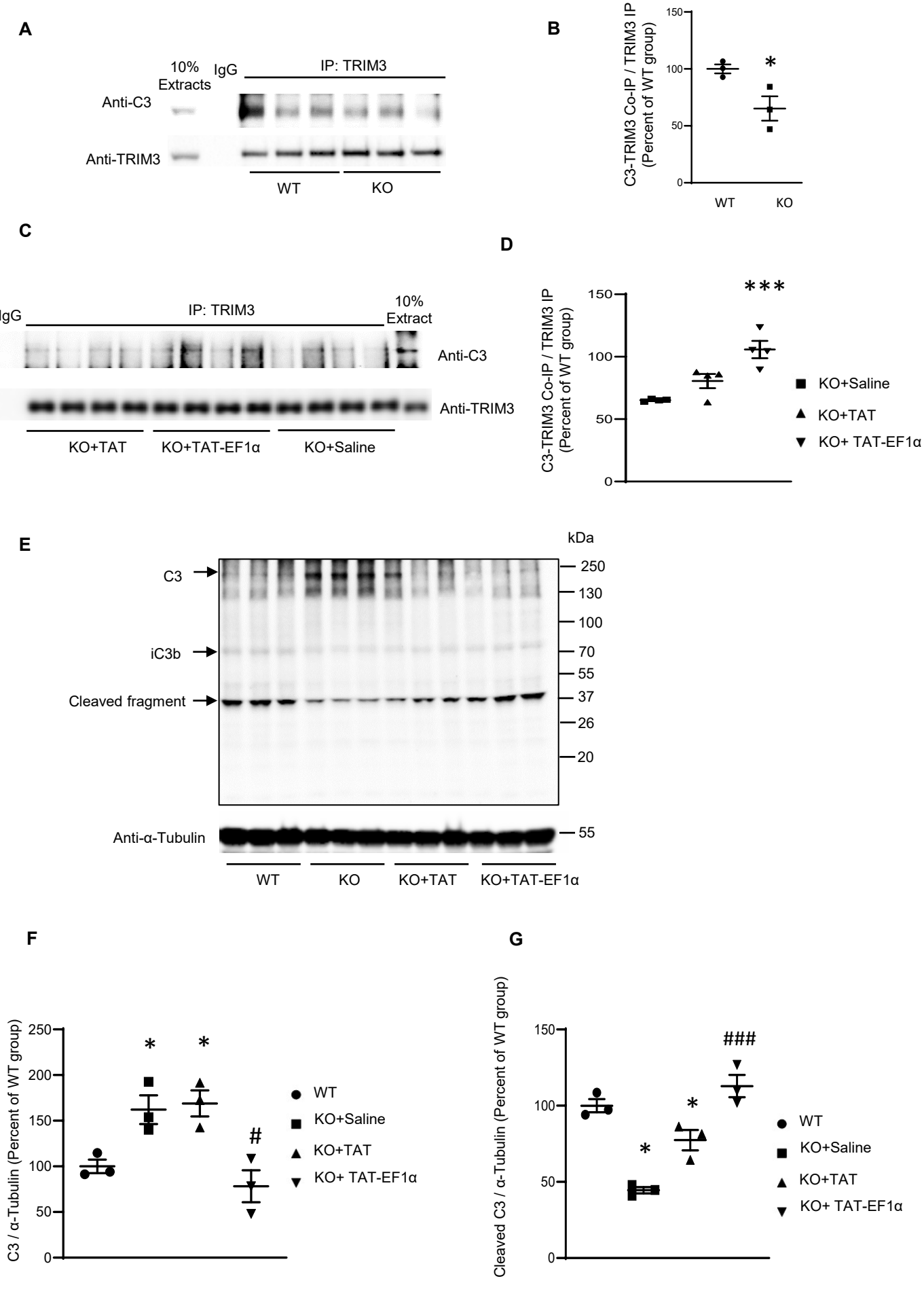

Su et al., 2023 Figure 5-1

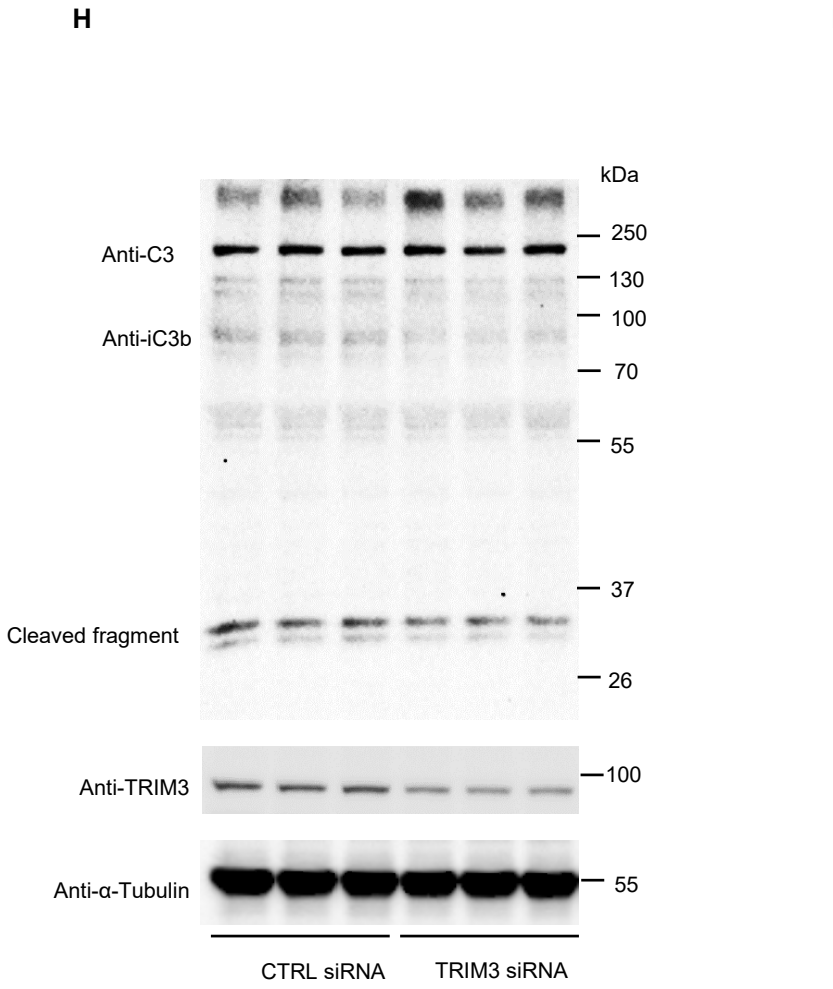
H
kDa
Anti-C3
Anti-iC3b
250
130
100
70
55
37
Cleaved fragment
26
Anti-TRIM3
100
Anti-α-Tubulin
55
CTRL siRNA
TRIM3 siRNA

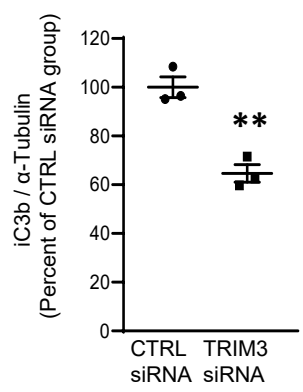
I
iC3b / α-Tubulin
(Percent of CTRL siRNA group)
120
100
80
60
40
20
0
**
CTRL siRNA
TRIM3 siRNA

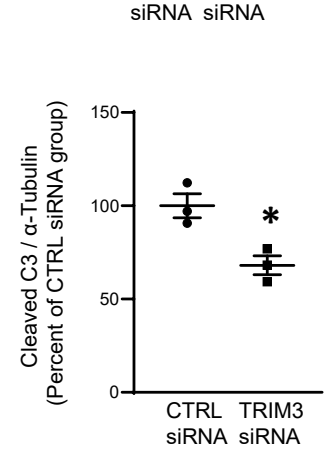
J
Cleaved C3 / α-Tubulin
(Percent of CTRL siRNA group)
150
100
50
0
*
CTRL siRNA
TRIM3 siRNA

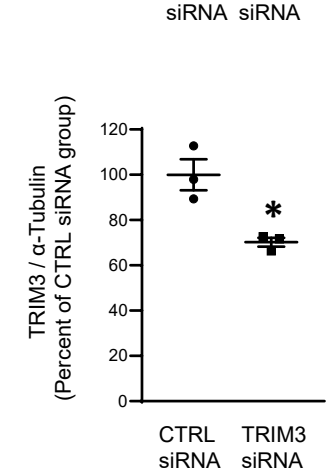
K
TRIM3 / α-Tubulin
(Percent of CTRL siRNA group)
120
100
80
60
40
20
0
*
CTRL siRNA
TRIM3 siRNA

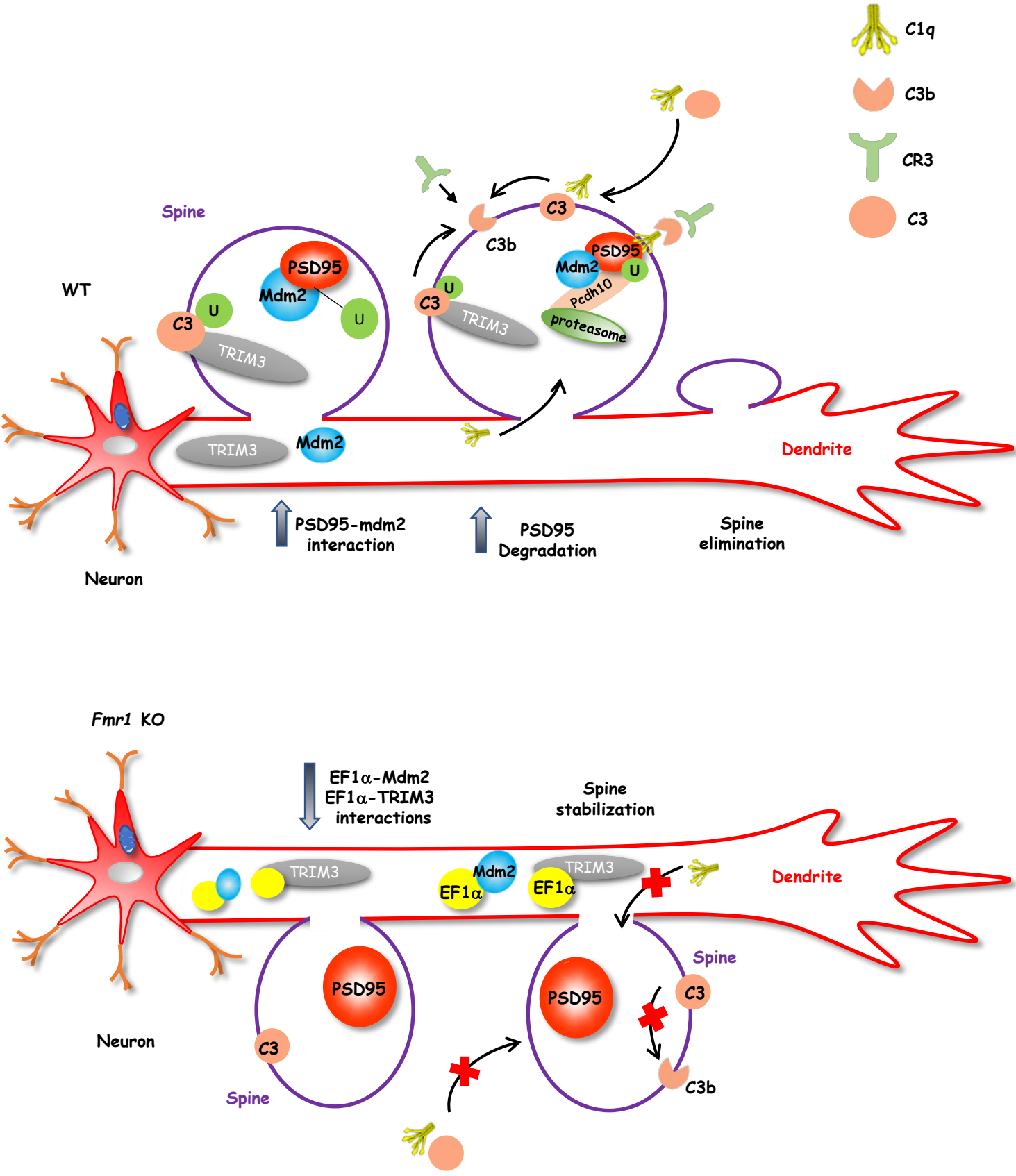

Su et al., 2023 Figure 6